Flow of ϕ mesons in pPb collisions at the LHC with the CMS detector

by

Mukund Madhav Varma

Submitted to the Department of Physics
in partial fulfillment of the requirements for the degree of

Master of Science in Physics

at the

MASSACHUSETTS INSTITUTE OF TECHNOLOGY

June 2015

Signature redacted

Author .....
Department of Physics
Mar 16, 2015

Signature redacted

Certified by .....
Professor Gunther Roland
Professor of Physics
Thesis Supervisor

Signature redacted

Accepted by .....
Professor Nergis Mavalvala
Associate Department Head for Educationr

Flow of ϕ mesons in pPb collisions at the LHC with the CMS detector

by

Mukund Madhav Varma

Submitted to the Department of Physics
on Mar 16, 2015, in partial fulfillment of the
requirements for the degree of
Master of Science in Physics

Abstract

Measurements of two-particle angular correlations between unidentified charged particles and ϕ-mesons are shown over a wide pseudorapidity range ($\Delta\eta < 2$) in pPb collisions. The data, collected during 2013 pPb run at a nucleon-nucleon center-of-mass energy of 5.02 TeV with the CMS detector, corresponds to a total integrated luminosity of aproximately $35nb^{-1}$. ϕ-mesons are reconstructed via their hadronic decay channel, $\phi \rightarrow K^{+}K^{-}$, for high multiplicity events. The observed two-particle long range correlations are quantified by the second-order fourier coefficients (v_2) as a function of transverse momentum. The v_2 of ϕ-mesons is compared to that of other identified particles, to study the mass ordering and quark number scaling effects in measurements of elliptic flow.

Thesis Supervisor: Professor Gunther Roland
Title: Professor of Physics

Acknowledgments

I would like to thank Gunther for giving me the opportunity to work on such an exciting frontier of physics, and for his help and guidance as my advisor. None of the work presented in this thesis would have been possible without Victoria and Yen-jie, who guided me through the intricacies of the analysis. I would also like to thank Bolek, Wit and George, whose probing questions helped me gain a clear understanding of the research I was doing. One of my favorite things about MIT was the community, and I probably learnt the most from my fellow grad students Last but not the least, I'd like to thank my parents and my friends - Akhilesh, Chiraag, Chris, Doga, Dragos, Sai, Suhrid, Vaibhav and Viral for their unwavering support and encouragement and of course, their pleasant company.

Contents

List of Figures

List of Tables

Chapter 1

Introduction

1.1 Fundamental Forces and Fundamental Particles

Nuclear and Particle physics in the present day deals with understanding fundamental particles, the most basic building blocks of nature, and the four fundamental forces that act between them.

All observable matter is made up of two kinds of fundamental particles called Quarks and Leptons. These particles decay and interact with each other in a variety of ways that are governed by the four fundamental forces. Figure 1-1 shows the different fundamental particles that make up all observable matter in the universe. Table 1.1 compares the comparitive strengths and ranges of the fundamental forces that govern their interactions.

Gravity, the weakest of the four, acts between massive bodies over large distances. Isaac Newton, in his masterpiece "Principia", first described the inverse square dependence of the gravitational force, building on the foundations laid by Galileo and Kepler. Much later, Albert Einstein would come up with the General Theory of Relativity, a more complete theory of gravity, yet one that is still not very well integrated with the rest of the forces.

Despite the success in understanding gravity in the early days of modern physics, we have not yet been able to integrate it with the other three fundamental forces. The theory which describes the Weak force, the Electromagnetic force and the Strong

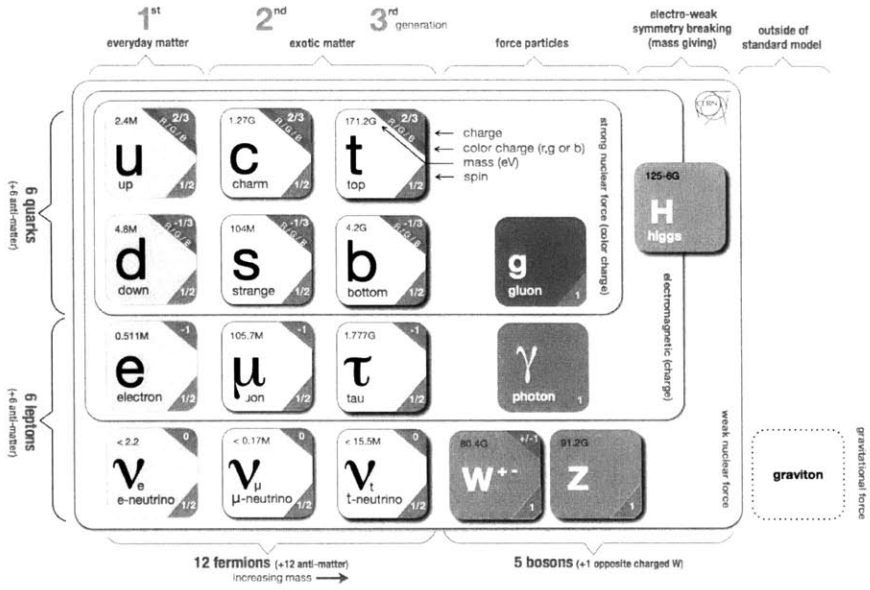

Figure 1-1: Fundamental particles in the Standard Model of Particle Physics (image from isgtw.org)

force is called the Standard Model of particle physics. The weakest of these, the Weak nuclear force deals with changes in "flavor" of quarks and leptons. In the Standard Model, the Weak force is mediated by the exchange of W and Z bosons.

The next strongest force is the Electromagnetic force. This is perhaps the best understood of all the four fundamental forces, as is evident from all the technology that is based on it. The first complete theory of Electromagnetism was proposed by James Maxwell, in the form of the famous Maxwell's equations. This force acts between electrically charged particles. Dirac, Feynman et al would go on to formulate it as a U(1) gauge theory called Quantum Electrodynamics(QED), with the photon as the mediating particle. At high energies, the Electromagnetic force is unified with the Weak Force. The theory describing the EM force and the Weak Force together is also known as the GSW theory in honor of its discoverers, Glashow, Salam and Weinberg.

The strongest of the fundamental forces is named the Strong Force. The strong force is responsible for holding the nuclei of atoms together as well as the constituents

of nucleons together! The theory which describes the strong force is called Quantum Chromodynamics (QCD) and is a SU(3) gauge theory with gluons being the gauge bosons. Gluons carry color charge, in contrast to photons which do not carry electric charge. An interesting consequence of this is that gluon-gluon interactions are possible which leads to many interesting phenomena that can be explored in QCD systems, some of which shall be explored in this thesis.

	Relative Strength	Range (m)	Mediating particle
Strong Force	1	10^{-15}	Gluon
Electromagnetic Force	1/137	Infinite	Photon
Weak Force	10^{-6}	10^{-18}	$W^{\pm}$, Z
Gravitational Force	10^{-39}	Infinite	?

Table 1.1: Relative strengths and ranges of the Fundamental Forces

1.2 Quantum Chromodynamics

Advances in experimental particle physics after the second world war saw the discovery of an entire "zoo" of subatomic particles, and just as with the periodic table in the previous century, a need was felt to organize these different particles somehow. A solution was found by Murray Gell-Mann with the Quark model which described these newly discovered hadrons as being made up of quarks and anti-quarks of 3 "flavors" - up, down and strange. The theory was experimentally validated by the discovery of the Ω^{--} baryon which was predicted by the quark model, but had not yet been observed in nature. A fourth quark, the charm quark was predicted by Glashow, Iliopoulos and Maiani, and its existence verified by the discovery of the J/Ψ meson by Samuel Ting and Burton Richter in 1974. The bottom quark was theorized by Koboyashi and Masakway in 1973 and discovered by the F288 experiment at Fermilab via the bottomonium. The final piece of the puzzle, the top quark was discovered much later, in 1995 by the CDF and D0 experiments, when advances in accelerator technology made it possible to reach the energies required to produce it.

The quark model, while providing an elegant explanation for the abundance of subatomic particles, only explained the composition of subatomic particles and not

their interactions. The theory that describes the interactions between quarks and gluons is known as Quantum Chromodynamics. In analogy to QED, where the charge associated with the Electromagnetic force is the electric charge, the charge associated with the Strong force is termed as the color charge. The color charge can come in three variants which we term blue, red and green; and they each have their anti-color. Every quark has a color associated with it, while each gluon carries a color and an anti-color. The gluons, thus, as mediators transfer color charge between quarks (and each other).

1.2.1 Quark confinement and asymptotic freedom

Two very interesting properties of the strong nuclear force stand at the root of many interesting phenomena being probed by nuclear and particle physicists today. Quark confinement, to put it simply, means that one can never observe a "free" quark in nature. They either exist as color-neutral quark-antiquark pairs (that we call mesons) or as triplets of quarks (baryons). Asymptotic freedom can be understood as being the property that at very small distances, the strength of the coupling between quarks decreases and they behave as if they were almost free.

Both these properties become clearer if we look at a graph of the strong coupling constant $\alpha_s(Q)$, as a function of the momentum transfer Q. As can be seen in Figure 1-2, at high values of Q, which correspond to short distances, the coupling constant becomes very small, so the colored objects experience a comparitively weaker force towards each other, while at large distances, the coupling constant becomes large, which means it becomes harder and harder to "pull apart" two or more quarks. One explanation for quark confinement is, that at some point the energy required to pull two quarks further away from each other becomes so large that it becomes more viable to create a new quark-antiquark pair from vacuum.

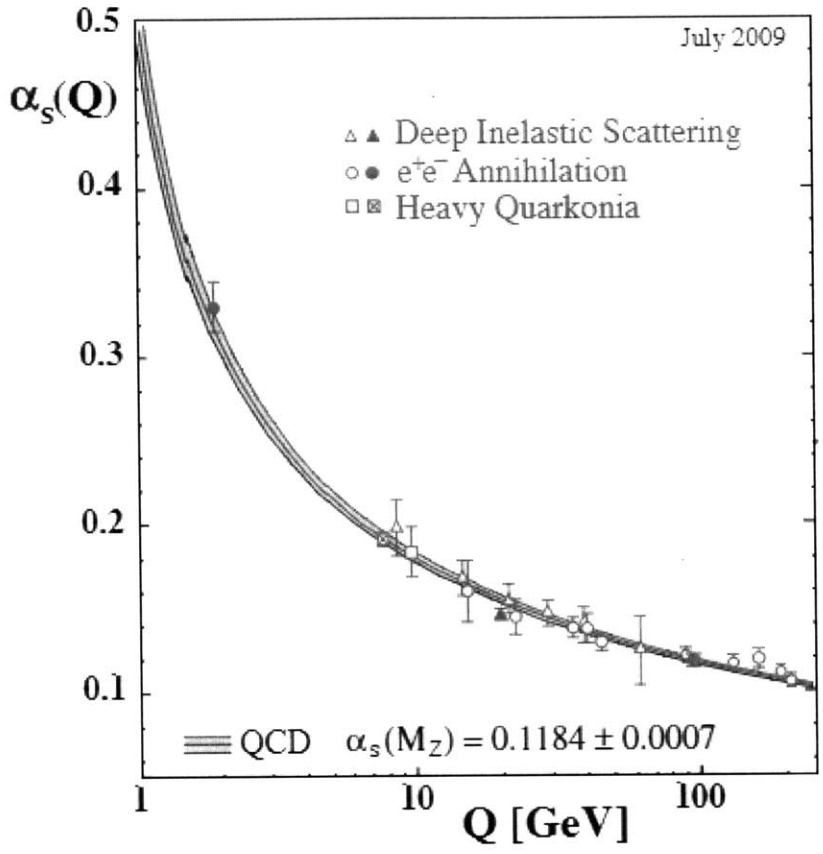

Figure 1-2: The coupling constant $\alpha_s(Q)$ as a function of momentum transfer Q[2]

1.2.2 QCD phase diagram and the Quark Gluon Plasma

Before we dive into the implications of the properties of the strong force discussed above, it is important to take a look at the QCD phase diagram. One of the most common examples of a "phase diagram" is that of water, which is usually drawn with Temperature and Pressure as the axes. The curves on such a plot represent the transition from steam to water, water to ice and steam to ice. The areas cordoned off by the curves represent the different phases. A similar diagram can be drawn for QCD matter, depicting the various phases that quark matter can exist in.

The QCD phase diagram is usually drawn with the baryon chemical potential(μ_B) and temperature (T) as axes, and is shown in Figure 1-3. However, unlike the phase diagram for water, the QCD phase diagram is not understood completely either theo-

retically or experimentally. One of the goals of modern experimental nuclear physics is to characterize the different regions. Baryon chemical potential can be thought to be a measure of net baryon density. The low temperature, low μ_B region thus corresponds to the hadronic phase, which is the everyday matter that we see and interact with. High chemical potential (density) and low temperatures correspond to cold nuclear matter found in neutron stars. In such cases, the phase transition into a "color-superconducting" state is believed to occur.

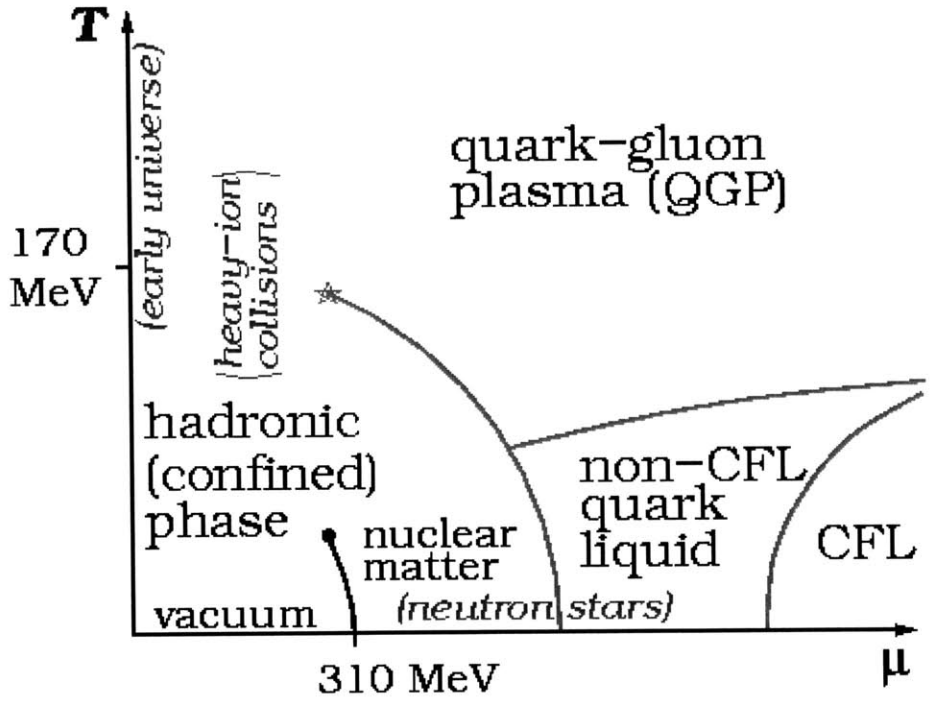

Figure 1-3: The QCD phase diagram (image courtesy wikipedia.org)

At the other end of the spectrum is a phase with high temperatures. As we keep on increasing the temperature, while keeping the baryon chemical potential roughly the same, we create more and more vacuum excitations giving rise to quark-antiquark pairs. At a certain temperature (termed the critical temperature, T_c), the distance between these hadrons becomes so small that they become essentially deconfined. This state was termed as the Quark-Gluon Plasma.

1.3 Heavy Ion Physics

One way to attain the temperatures and densities required to create a quark gluon plasma is to collide heavy ions together. Ions of Lead and Gold, for example, contain a large amount of nuclear matter, and accelerating them to high velocities provides the energy required to create hot dense states of quark matter. Historically, these collisions have been studied at Super Proton Synchrotron (SPS) at CERN and the Alternating Gradient Synchrotoron (AGS) at BNL. Today, these accelerators are succeeded by the Large Hadron Collider (LHC) at CERN, which plays host to the CMS experiment (on which this thesis is based) and the Relativistic Heavy Ion Collider (RHIC) at BNL.

1.3.1 Experimental goals of heavy ion physics

The goal of heavy ion physics, in a nutshell, is to relate the particles observed in the detector as a result of collisions of heavy ions, to the hot dense initial state believed to be formed immediately thereafter. To investigate the physics that links this initial state to the final state, some of the questions that heavy ion physicists are seeking to answer are:

- Is the medium quarkonic or hadronic in nature?
- Does the medium display collective behavior?
- How quickly does the medium thermalize?
- What are the thermodynamic and fluidic properties of the medium that is formed?
- What are the mechanisms for energy loss in this medium?

The observables that heavy ion physicists work with are the characterstics (position, momentum, energy etc.) of the particles produced in our detector. One way to use these observables to answer the fundamental questions listed above is to investigate the correlations of pairs of particles.

1.3.2 Collectivity and correlations in pA and AA collisions

Angular correlations of particles have been used as a tool in heavy ion physics to explore collective behavior in various systems and at various energies at RHIC [3, 4, 5, 6, 7] and LHC [8, 9, 10, 11, 12]. A system that does not reach thermal equilibrium while expanding will be much less correlated in the final state than a system that does. Qualititative evidence for this kind of collectivity in fixed target experiments was observed as early as the late 1970s to early 1980s. However, quantitative models failed to describe it until the operation of high energy heavy ion collision experiments at RHIC. At RHIC, finally, predictions of anisotropy and collective behavior in collision systems were successfully described using ideal fluid hydrodynamics. This was evidence that the QGP was far more liquid-like than previously thought of.

The primary driving force behind this research was an observation of long-range correlations in the azimuthal angle, including a "ridge"-like structure at $\Delta\varphi = 0$ (Figure 1-4), in nucleus-nucleus collisions. This implied that particles were found to be more likely to be produced at the same value of the azimuthal angle, φ (described in detail in chapter 2), but all along the length of the detector. The earliest explanations of this phenomena ascribed it to an almond shaped region of overlap being formed between two large nuclei in non-central collisions, which led to preferential emission of particles in the direction with the higher pressure gradient. However, the geometry-based explanation alone is insufficient to explain the presence of this phenomenon in collisions of two protons, or asymetric systems like a proton-nucleus collision. Many of the leading theoretical interpretations of this result ascribe this observation to collective hydrodynamic flow of a strongly interacting, expanding medium [13].

One of the first, and most exciting discoveries of the LHC was the observation of this "ridge" in high-energy, high-multiplicity proton-proton collisions as well [14]. The presence of this effect, while much less pronounced than in nucleus-nucleus collisions was still extremely important. The 2013 LHC pPb run was highly anticipated for providing a reference with which to compare these two very differently sized systems. The pPb run led to another exciting discovery with a relatively large effect being

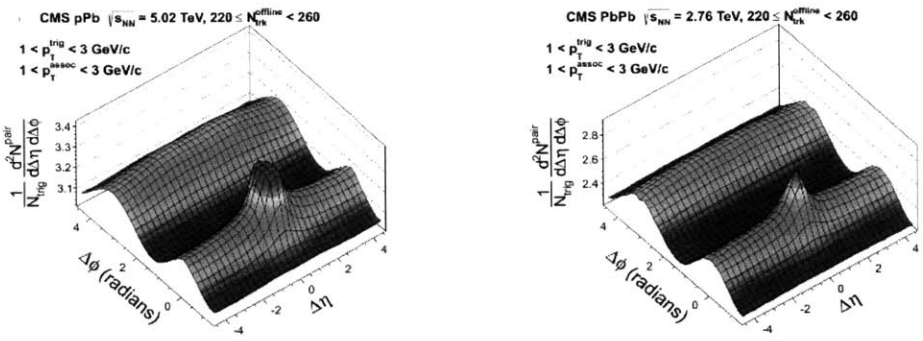

Figure 1-4: Observation of the "ridge"-like long-range correlations in pPb and PbPb collisions with CMS [8, 9]

observed in pPb collisions [15, 16, 17], which suggested that this effect might not be as dependent on system size, and hence collision geometry, as previously thought.

These anisotropies are quantified by Fourier decomposition of the azimuthal pair distribution [18]. Of particular interest are the second and third coefficients of this distribution, which are termed as the elliptic (v_2) and triangular (v_3) flow repectively.

A number of theoretical explanations have been proposed to account for this phenomenon [19]. The task at hand for experimental physicists, is now, to make measurements that will allow us to rule out one or more of these explanations.

1.3.3 Correlations of identified particles

One way to probe the origin of the azimuthal anisotropy observed in two-particle correlations is to look at correlations of identified particles.

Mass ordering

Measurements by the STAR [22] and PHENIX [23] experiments at RHIC revealed an interesting dependence of v_2 on the particle species. At transverse momenta $p_T <$ 2GeV, the v_2 of heavier particles was observed to be lower for the same p_T. This effect is termed as "Mass Ordering" and is explained as a result of stronger effect of radial flow on heavier particles in hydrodynamic models [24, 25, 26, 27, 28]. The radial flow shifts the p_T spectra of identified particles towards higher p_T's. For a given

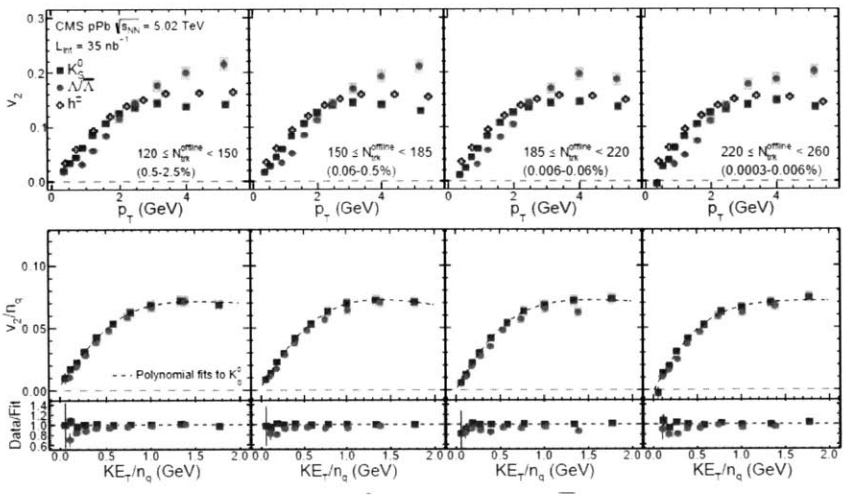

Figure 1-5: Elliptic flow (v_2) of K_s,$\Lambda/\bar{\Lambda}$ and all charged hadrons measured by the CMS experiment, demonstrating the quark number scaling and mass ordering effects [20]

value of the radial flow velocity of the expanding medium, more massive particles will experience a higher shift in their p_T spectra as compared to lighter particles. Intuitively, this can be visualized by considering that ideal hydrodynamics will boost all hadrons equally, and so hadrons with higher mass will have higher p_T for the same value of v_2, or to put it another way, lower v_2 for the same p_T. The ALICE and CMS experiments observed the mass ordering effect in pPb collisions [21, 20] at the LHC, which can also be described by hydrodynamics [29, 30].

Quark number scaling

In contrast, at intermediate p_Ts ($2 < p_T < 5$ GeV), baryons are observed to have a higher v_2 than mesons, and the v_2 Fourier harmonic as a function of the transverse kinetic energy ($KE_T = \sqrt{m_0^2 + p_T^2} - m_0$), scales with the number of constituent quarks n_q in a hadron. That is, if v_2/n_q is plotted as a function of KE_T/n_q for each type of mesons ($n_q = 2$) and baryons ($n_q = 3$), all curves will coincide. This phenomenon has been termed as "Constituent quark scaling" or "Quark number scaling", and can be thought to arise from the deconfined behavior of quarks in the QCD "fireball" [31, 32]. This simple scaling law may indicate that the elliptic flow is developed first among quarks before they recombine into hadrons [33, 34, 35], providing evidence of

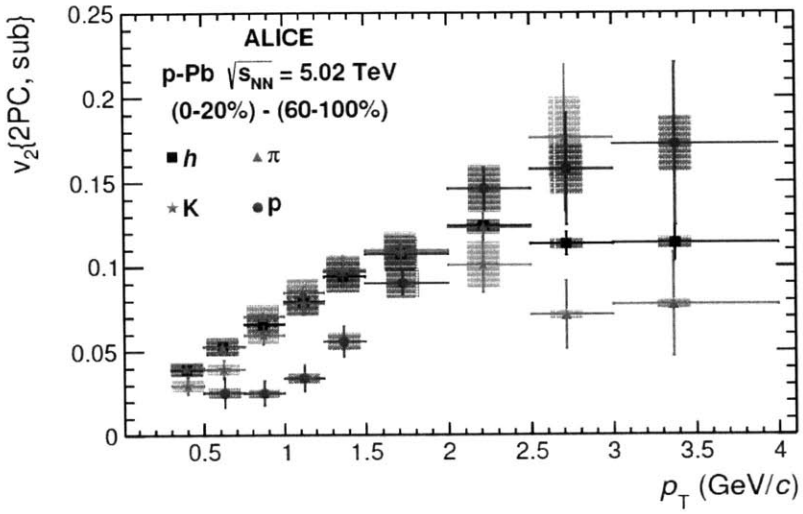

Figure 1-6: Elliptic flow (v_2) of K_s,$\Lambda/\bar{\Lambda}$, protons and all charged hadrons measured by the ALICE experiment, demonstrating the quark number scaling and mass ordering effects [21]

deconfinement of quarks and gluons in high-energy pA and AA collisions. It is of high interest to look for such quark number scaling of azimuthal correlations in smaller collision systems like pp and pPb.

The interplay of these two competing effects can be useful in differentiating models of the initial state and evolution of the quark-gluonn plasma.

1.3.4 The ϕ-meson as a probe of the Quark-Gluon Plasma

The ϕ-meson has some very interesting properties that make it a great candidate for exploring various aspects of heavy ion physics. High strangeness content has been suggested as a signature of the quark-gluon plasma, which makes it interesting to study the production of ϕ-mesons in heavy ion collisions. The ϕ also has a low hadronic cross-section of interaction, which suggests that most collective effects will arise at the partonic stage and remain unaffected by the hadronic rescattering phase. Moreover, with its (relatively) long lifetime, it is expected to decay outside the QCD fireball, hence carrying information from before the chemical freeze-out.

In addition, with regards to the elliptic flow of identified particles mentioned above,

Quark Content	$s\bar{s}$
Mass	$1019.46 MeV$
Decay Width	$4.26 MeV$
Lifetime	$1.55 \times 10^{-22} s$

Table 1.2: The ϕ-meson in a nutshell.

the ϕ-meson makes for a great differentiator being a meson with mass comparable to baryons like the proton and the Λ, allowing us to compare the validity of both the mass ordering and constituent-quark scaling effects with a single proble. In this thesis, we shall make measurements of the v_2 for ϕ-mesons to explore the origin of flow in pPb and PbPb collisions.

Chapter 2

The CMS Experiment

The CMS experiment consists of the CMS (Compact Muon Solenoid) detector installed at the Large Hadron Collider at CERN. The CMS experiment proved to be extremely successful at its original purpose - the study of electroweak symmetry breaking due to the Higgs mechanism. Some of the features which enabled CMS to be so successful - good charged-particle momentum resolution and reconstruction efficiency, wide geometric coverage, and precise electromagnetic energy resolution - also make it a great detector for studying heavy ion physics. Many of the most interesting discoveries in heavy ion physics in recent years have come out of the LHC and the CMS experiment [14, 36, 8, 9, 15, 37, 20]. In the next few sections, the CMS detector is described in brief, with details about the parts of the detector most relevant to the topic of this thesis.

2.1 CMS Detector

The layout of the CMS detector is shown in Figure2-1 . The solenoid in the name of the CMS detector is a superconducting magnet. The different sub-detector systems of the CMS detector are surrounded by this solenoid, which provides a uniform magnetic field of strength $3.8T$ throughout its volume. The major components of the detector include the pixel tracker, the silicon-strip tracker, the brass-scintillator hadronic calorimeter (HCAL) and the lead-tungstate crystal electromag-

netic calorimeter (ECAL). Figure2-2 shows a slice of the CMS detector, depicting the arrangement of the different sub-detectors within CMS. In addition, there are the crystal/quartz-fibre hadron forward calorimeters in the forward region ($2.9 < \eta < 5.0$).

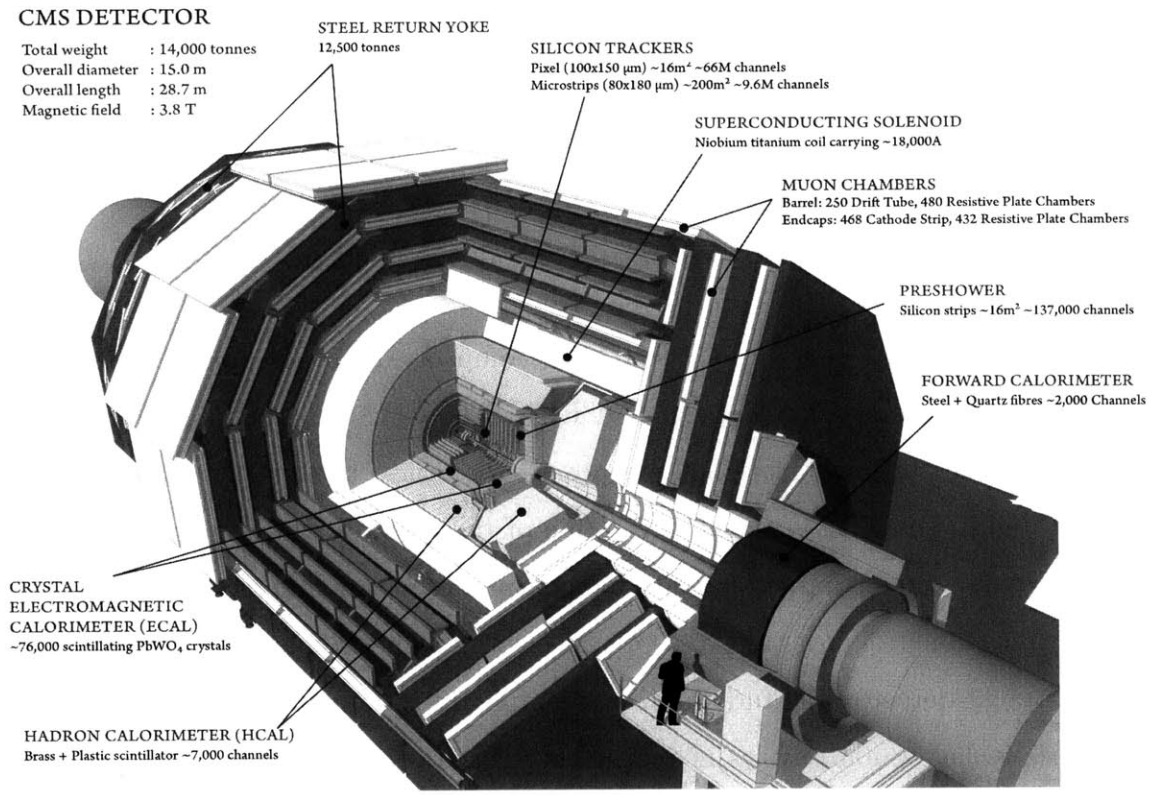

Figure 2-1: Sectional view of the CMS detector showing the various components

For the purpose of the research discussed in this thesis, we require high-precision measurement of the momentum and position of the particles produced in heavy ion collisions. Experimentally, this amounts to measuring with accuracy the paths or "tracks" of the produced particles. This is made possible in part by the powerful magnetic field, which causes charged particles to bend more, and allows us to get a better resolution on our measurement. The most relevant hardware components of the CMS detector for this thesis are the pixel tracker, and the silicon strip tracker, which together constitute the inner tracking system of CMS. On the software side, better tracking algorithms allow us to better "join the dots" of the electrical signals left by charged particles in the detector. Another aspect of the experiment crucial

to this analysis is the triggering system which we use to select interesting events (events that produce a high multiplicity of particles, in our case). The tracker and the triggers are discussed in sections 2.1.2 and 2.2, while the track reconstruction is discussed in section 3. We begin by describing the coordinate system used for measuring observables in the detector.

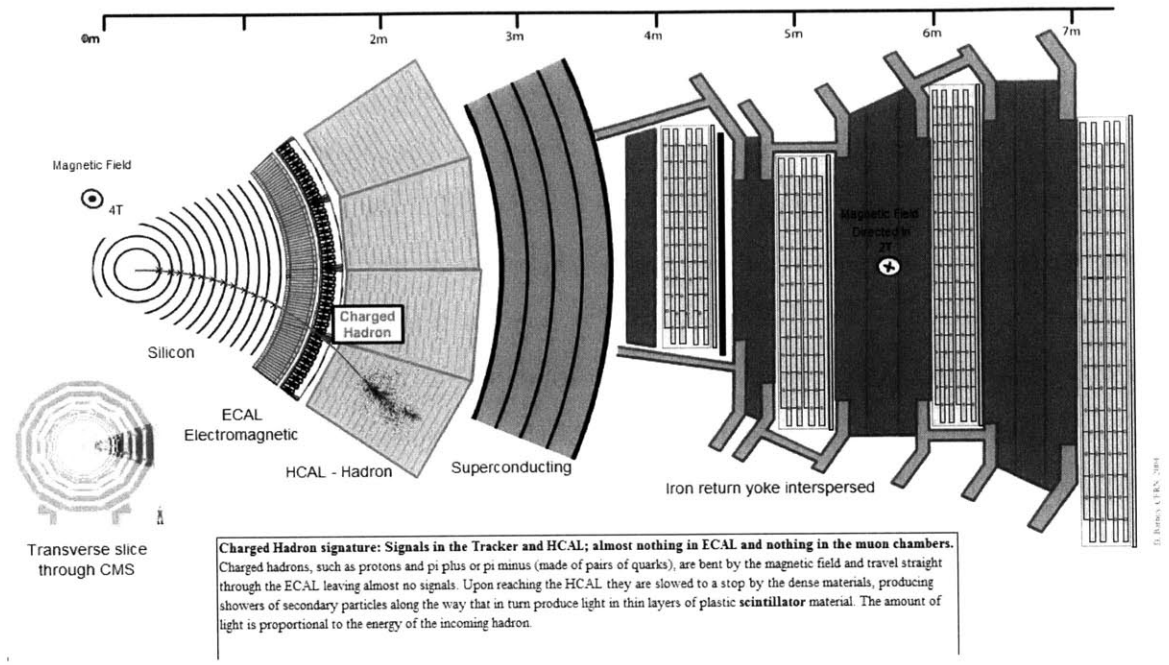

Figure 2-2: Transverse slice of the CMS detector, showing detection of charged hadrons

2.1.1 Coordinate System

As can be seen in Figure2-1, the detector is a cylinder centered around the beam on which the accelerated particles collide. The particles that are produced in these collisions are detected along the surface of this cylinder by the various subsystems of the detector. The positions of particles in the detector are mapped on to a plane that can be constructed by unfolding this cylindrical surface into a plane. The origin of this plane is taken to be at the interaction point. Any position on this plane can be described in terms of the azimuthal angle ϕ which has its 0 at the x-axis (pointing to the center of the LHC in the right-handed cartesian coordinate system), and the

pseudorapidity η which is a measure of how far along the beam this position is. We use the pseudorapidity instead of simply the z coordinate or the polar angle θ since it is relativistically invariant. The pseudorapidity is related to the polar angle by the relation $\eta = -log(tan(\theta/2))$.

2.1.2 Inner Tracking

The inner tracking system of CMS is made up of two sub-detector systems, the pixel tracker, which is the sub-detector situated closest to the beamline, and the silicon-strip tracker, which comes next. In all, it consists of 1,440 silicon pixel and 15,148 silicon strip detector modules. The silicon tracker measures charged particles within the pseudorapidity range $|\eta| < 2.5$, and provides an impact parameter resolution of $\approx 15\mu m$ and a transverse momentum (p_T) resolution better than 1.5% up to $p_T \approx 100$ GeV/c. Figure 2-3 shows the configuration of the various silicon strip layers and the pixel detector in the $\eta - r$ space.

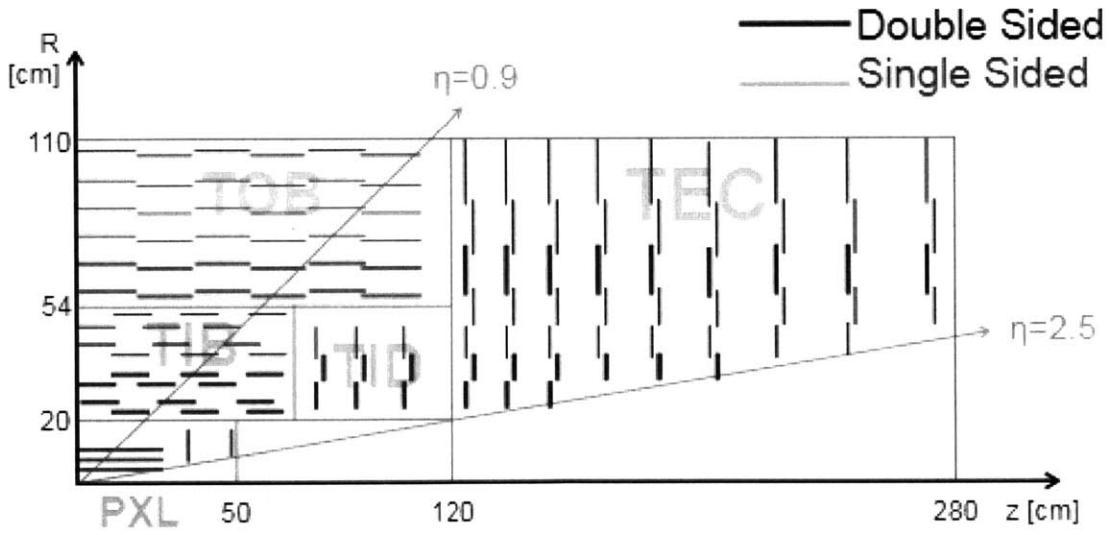

Figure 2-3: Schematic of the different subdetectors in the tracker[38]

This combination of detectors allows us to measure charged particle tracks up to a pseudorapidity of $|\eta| < 2.5$ providing near hermetic coverage of the detector.

Pixel Detector

The pixel detector is divided into three barrel layers of length 53 cm and radius 4.4 cm, 7.3 cm and 10.2 cm; and two pairs of endcap disks situated at $|z| = 34.5$ cm and 46.5 cm. A schema of the geometry is shown in Figure 2-3.

The pixel detector is made up of 66 million pixels of size $100 \times 150\ \mu m^2$. The read out from these channels is handled by a zero-suppression scheme with analog pulse height read-out. The zero-suppression reduces the readout volume by removing channels with no signal. The analog pulse height read-out helps to separate signal and noise hits and identify large hit clusters from overlapping tracks. The charge sharing helps to improve position resolution.

Silicon Strip Detector

The silicon strip detector is the next detector going outwards from the beam line. The barrel region of the detector ranges from a radius of 20 cm to 110 cm over a length of $|z| < 110$ cm. Its different parts of the detector are the Tracker Inner Barrel (TIB), the Tracker Outer barrel (TOB) and the Tracker Inner Disks (TID). In addition, the Tracker End-Cap disks extend over a range 120cm $< |z| <$ 280 cm, extending the total coverage to $|\eta| < 2.5$.

2.1.3 Electromagnetic (ECAL) and Hadronic (HCAL) Calorimeters

The Electromagnetic calorimeter (ECAL) and Hadronic calorimeter (HCAL) are responsible for measuring the energy deposited by electrons and photons (for the ECAL) and hadrons (for the HCAL) respectively. Energy measurements, while especially crucial in studies of jets, aren't directly used in flow measurements. However, it is important to introduce the calorimeters because of the role they play in the trigger system, which shall be discussed in the next section.

The ECAL consists of Lead Tungstate crystals, which act as scintillators towards the passage of electrons and photons. They have a short radiation length ($X_0 =$

0.89 cm) and a Moliere radius of 2.2 cm. Avalanche photo-diodes (APDs) are used to capture the light in the barrel region of the detector, while vacuum phototriodes (VPTs) are used in the end-cap region.

The HCAL consists of plastic scintillator and brass absorbers.

2.2 Triggering

Due to the high luminosity of the collisions at the LHC (peak instanteous luminosity of 80-120 Hz/mb for pPb collisions), more than a hundred thousand pPb collision events happen every second (assuming an inelastic cross section of interaction between proton and Lead of 2 barns[39]). With the electronics technology we have at present, it is impossible to record data from each event. To this end, we only write a fraction of this data to tape using the CMS trigger system. There are different types of triggers used to select events that can be interesting to us for exploring various physics problems, like an event with a high transverse momentum jet, or an event which produces many particles.

These triggers are implemented in two stages - the Level 1 (L1) trigger at the hardware level, and High-level trigger (HLT) at the software level. The L1 trigger operates on the output of the detector hardware, which means that it fires when a signal is detected in the calorimeters or the muon system. The HLT trigger on the other hand works at the software level. It comprises of a computing farm which performs a full reconstruction on each event selected by the L1 trigger. Events that pass the HLT triggers are then stored offline for use in physics analyses.

2.2.1 MinBias Trigger

Minimum bias pPb events are triggered by requiring at least one track with $p_T > 0.4$ GeV to be found in the pixel tracker for a pPb bunch crossing. Because of hard-ware limits on the data acquisition rate, only a small fraction (10^{-3}) of all minimum bias triggered events are recorded.

2.2.2 High Multiplicity Trigger

In order to collect a large sample of high-multiplicity pPb collisions, a dedicated high-multiplicity trigger is also implemented using the CMS Level 1 (L1) and high-level trigger (HLT) systems. At L1, two event streams were triggered by requiring the total transverse energy summed over ECAL and HCAL to be greater than 20 or 40 GeV. Charged tracks are then reconstructed online at the HLT using the three layers of pixel detectors, and requiring a track origin within a cylindrical region of 30 cm length along the beam and 0.2 cm radius perpendicular to the beam. For each event, the number of pixel tracks (N_{trk}^{online}) with $|\eta| < 2.4$ and $p_T > 0.4$ GeV is counted separately for each vertex. Only tracks with a distance of closest approach of 0.4 cm or less to one of the vertices are included. The online selection requires N_{trk}^{online} for the vertex with the most tracks to exceed a specific value. Data are taken with thresholds of $N_{trk}^{online} > 100$, 130 (from events with L1 threshold of 20 GeV), and 160, 190(from events with L1 threshold of 40 GeV). While all events with $N_{trk}^{online} > 190$ are accepted, only a fraction of the events from the other thresholds are kept. This fraction is dependent on the instantaneous luminosity. Data from both the minimum bias trigger and high-multiplicity trigger are retained for offline analysis.

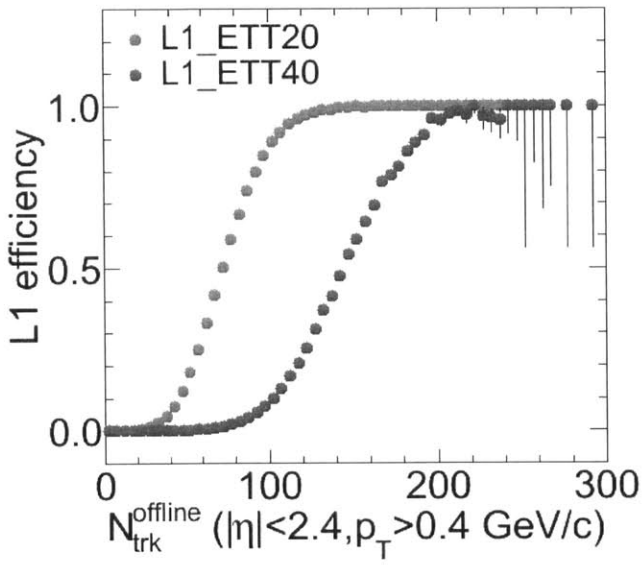

Figure 2-4: L1 efficiency as a function of offline track multiplicity, N_{trk}^{off}, for the two L1 seeds used in the first four threshold HLT triggers.

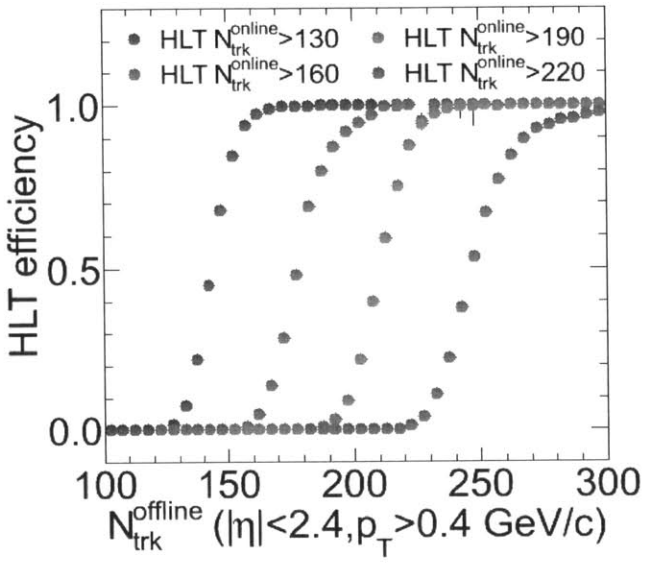

Figure 2-5: HLT trigger efficiency as a function of offline track multiplicity, for the top four most selective high multiplicity triggers.

2.3 Event Selection

In the offline analysis, hadronic collisions are selected by the presence of at least one tower with energy above 3 GeV in each of the two HF calorimeters. Events are also required to contain at least one reconstructed primary vertex within 15 cm of the nominal interaction point along the beam axis and within 0.15 cm transverse to the beam trajectory. At least two reconstructed tracks are required to be associated with the primary vertex, a condition that is important only for minimum bias events. Beam related background is suppressed by rejecting events for which less than 25% of all reconstructed tracks pass the high-purity selection (as defined in Ref. [48]).The pPb instantaneous luminosity provided by the LHC in the 2013 run resulted in a 3% probability of having at least one additional interaction present in the same bunch crossing (pile-up events). The procedure used for rejecting pile-up events is described in [37] and is based on the number of tracks associated with each reconstructed vertex and the distance between different vertices. A purity of 99.8% for single pPb collision events is achieved for the highest multiplicity pPb interactions studied in this paper. With the selection criteria above, 97 to 98% of the events are found to be selected

among those pPb interactions simulated with the EPOSLHC and HIJING 2.1 event generators that have at least one particle from the pPb interaction with energy E >3 GeV in each of the η ranges $3 < |\eta| < 5$. In this analysis, *CMS highpurity* tracks are used to select primary tracks (tracks originating from the pPb interaction). Additional requirements are applied to enhance the purity of primary tracks. The significance of the separation along the beam axis (z) between the track and the best vertex,$d_z/\sigma(d_z)$, and the significance of the impact parameter relative to the best vertex transverse to the beam $d_T/\sigma(d_T)$, must be less than 3, and the relative p_T uncertainty, $\sigma(p_T)/p_T$, must be less than 10%. To ensure high tracking efficiency and to reduce the rate of misreconstructed tracks, primary tracks with $|\eta| < 2.4$ and $p_T > 0.3$ GeV are used in the analysis (a p_T cutoff of 0.4 GeV is used in the multiplicity determination to match the HLT requirement). The total reconstruction efficiency for primary track reconstruction exceeds 60% for $p_T < 0.3$ GeV and $|\eta| < 2.4$. The efficiency is greater than 90% in the $|\eta| < 1$ region for $p_T > 0.6$ GeV [37].

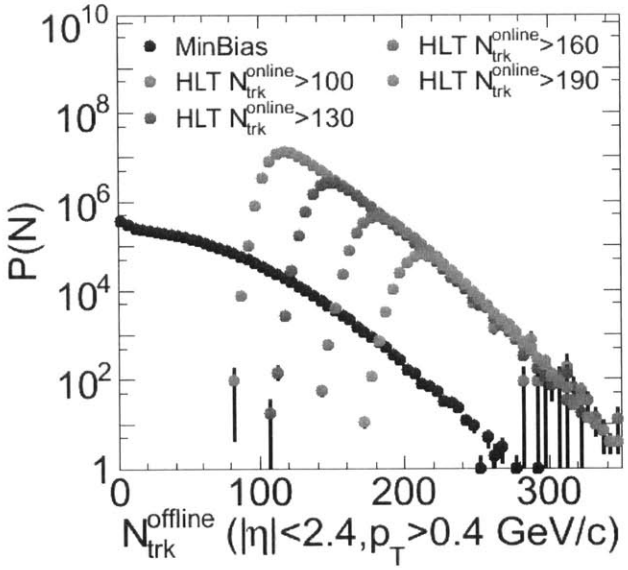

Figure 2-6: N_{trk}^{off} spectra for minimum bias and for all the different high multiplicity trigger paths are shown after applying pileup rejection.

Table 2.1: Fraction of the full event sample in each multiplicity bin and the average multiplicity per bin for pPb data.

Multiplicity bin (N_{trk}^{off})	Fraction	$\langle N_{trk}^{off} \rangle$	$\langle N_{\mathrm{trk}}^{\mathrm{corrected}} \rangle$
MB	1.00	40	50±2
[0, 20)	0.31	10	12±1
[20, 30)	0.14	25	30±1
[30, 40)	0.12	35	42±2
[40, 50)	0.10	45	54±2
[50, 60)	0.09	54	66±3
[60, 80)	0.12	69	84±4
[80, 100)	0.07	89	108±5
[100, 120)	0.03	109	132±6
[120, 150)	0.02	132	159±7
[150, 185)	4×10^{-3}	162	195±9
[185, 220)	5×10^{-4}	196	236±10
[220, 260)	6×10^{-5}	232	280±12
[260, 300)	3×10^{-6}	271	328±14
[300, 350)	1×10^{-7}	311	374±16

2.4 Data and Monte Carlo Samples

The data sample used in this analysis was collected with the CMS detector during the LHC pPb run in 2013. The total integrated luminosity of the data set is about $35nb^{-1}$. The beam energies are 4 TeV for protons and 1.58 TeV per nucleon for lead nuclei, resulting in a center-of-mass energy per nucleon pair of 5.02 TeV. The direction of the proton beam was initially set upto be clockwise ($20nb^{-1}$), and was later reversed ($20nb^{-1}$). As a result of the energy difference between the colliding beams, the nucleon-nucleon center-of-mass in the pPb collisions is not at rest with respect to the laboratory frame. Massless particles emitted at $\eta_{CM} = 0$ in the nucleon-nucleon center-of-mass frame will be detected at $\eta_{CM} = +0.465$ (clockwise proton beam) or -0.465(counterclockwise proton beam) in the laboratory frame.

pPb collision events simulated with the HIJING (1M MinBias events) and EPOS-LHC (5M MinBias events) generators are used for closure tests which require comparison of generator-level truth to the detector-level observations. These tests are described in further sections.

Chapter 3

Track selections and performance

The track selection and performance studies presented in the following sections are common to all CMS analyses that make use of the tracking. These studies are crucial to understanding the limitations of CMS tracking on our results, and thus a collection of the most salient studies has been presented here. A detailed description of the CMS track reconstruction and tracking performance studies can be found in references [40, 38].

3.1 Track selections

The standard CMS combinatorial track finder (CTF) has a high efficiency to find tracks, but it contains quite a large fraction of fake tracks. The fake rate can be effectively reduced by applying a set of tracking quality cuts. The optimized standard set of tracking quality selections in CMS is known as "highPurity" tracks. In this analysis, the official CMS *highPurity* [41] tracks were used. For further selections, a reconstructed track was considered as a primary-track candidate if the impact parameter significance $d_{\mathrm{xy}}/\sigma(d_{\mathrm{xy}})$ and significance of z separation between the track and the best reconstructed primary vertex (the one associated with the largest number of tracks, or best χ^2 probability if the same number of tracks is found), $d_z/\sigma(d_z)$, are both less than 3. In order to remove tracks with poor momentum estimates, the relative uncertainty of the momentum measurement $\sigma(p_T)/p_T$ was required to

be less than 10%. Primary tracks that fall in the kinematic range of $|\eta| < 2.4$ and $p_T > 0.1\ GeV/c$ were selected in the analysis to ensure a reasonable tracking efficiency and low fake rate.

3.2 Comparison of Simulation to Data

A Monte Carlo (MC) is used in this analysis to correct for detector reconstruction effects, particularly on the track reconstruction. While we do not expect to see exactly the same results in Monte Carlo simulations and real physics data, the simulations can still be used to help characterize the detector performance. Figure 3-1 through 3-12 show some direct comparison plots of the Monte-Carlo simulations compared to the data it is useful to check if the detector simulations are comparable to data. Only tracks which passed the $N_{trk}^{offline}$ selection cuts and a $z_{\text{vtx}} < 0.15$cm where shown. The track variable were also weighted such that the normalized z_{vtx} distributions in MC and data matched.

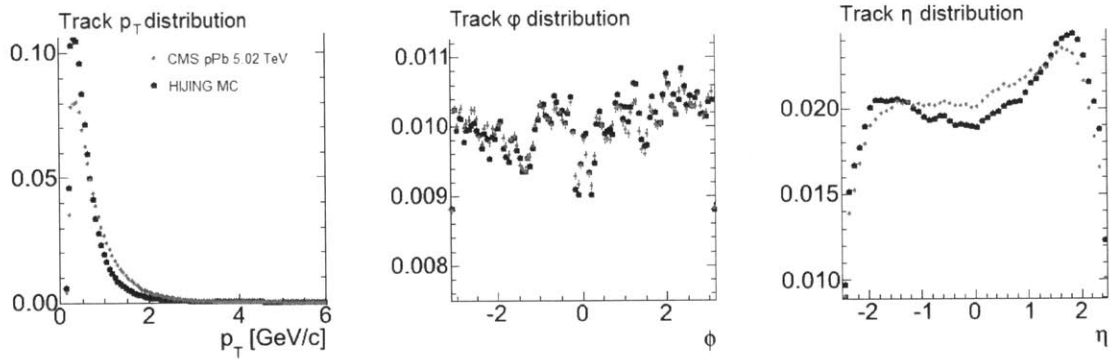

Figure 3-1: The p_T, η, and ϕ distributions for pPb data and HIJING MC are shown.

3.3 Tracking performance

The performance of the tracking is evaluated based on the matching of reconstructed tracks and TrackingParticles based on the fraction of shared hits. The absolute efficiency, which is the algorithmic efficiency multiplied by the geometric acceptance, was studied.

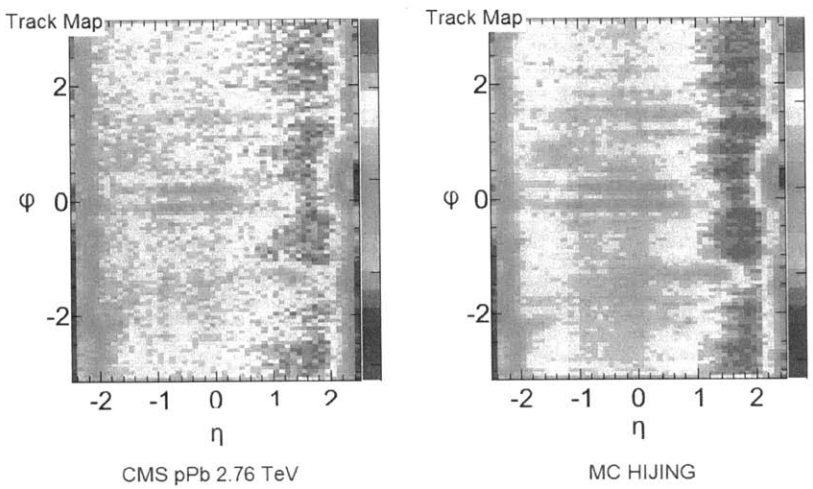

Figure 3-2: The $\eta - \phi$ distribution of tracks from data and HIJING MC are shown

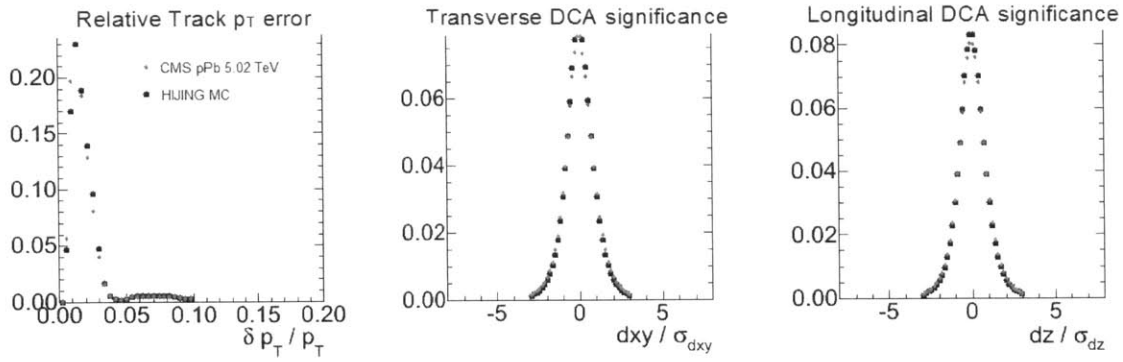

Figure 3-3: Track quality variables corresponding to the relative p_T uncertainties, the DCA in the transverse as well as the z directions for pPb data and HIJING MC are shown.

The Figures 3-5 through 3-10 on the following pages show projections of the tracking performance in pseudorapidity (η) and transverse momentum (p_T) based on MC samples from HIJING pPb simulations. This provides a good reference for the actual data, as can be seen above.

As a cross check of the tracking efficiency, the calculations were repeated for PYTHIA simulations. The absolute efficiency comparison between PYTHIA, HIJING, and HYDJET is shown in Figure 3-11. The efficiencies are shown as a function of η for $0.3 < p_T < 12\ GeV/c$ (left) and p_T with $|\eta| < 2.4$ (right). The HYDJET calculation only includes events with $N_{TP} < 200$ (the number of simulated tracks in each event) for reasons discussed in the next section. Both HIJING and PYTHIA

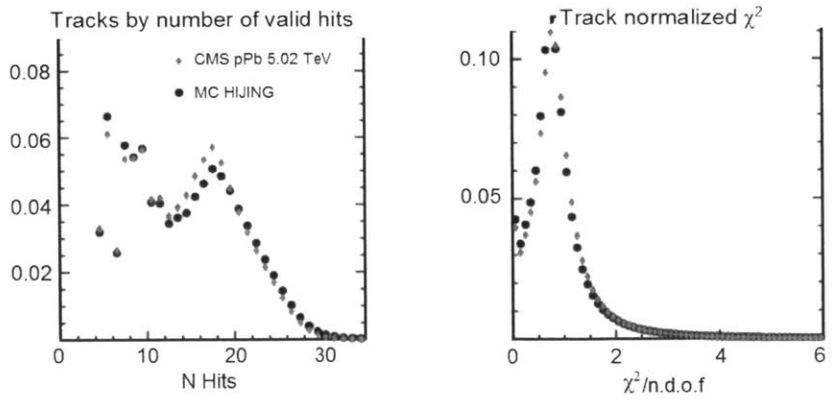

Figure 3-4: The track quality variables N_{hit}, the number of hits per track, and the χ^2 per d.o.f. for pPb data and HIJING MC are shown.

calculations were done in CMSSW 538patch3 and HYDJET was done in CMSSW 442patch5. A comparison of the fake rates from the three generators was also done and is shown in Figure3-12 with the same kinematic cuts.

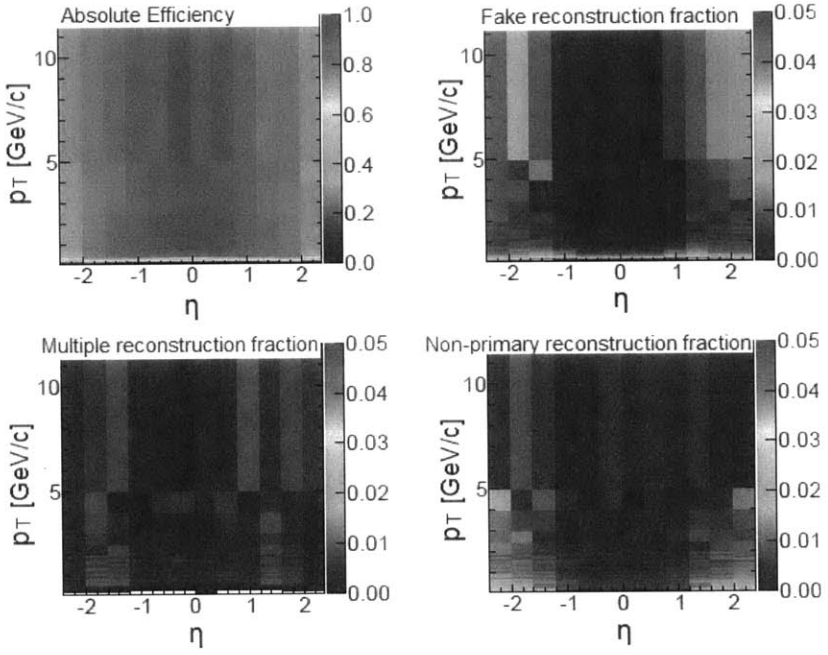

Figure 3-5: From left to right, and top to bottom, the plots of pseudorapidity versus transverse momentum are shown for: absolute tracking efficiency, fake track fraction, multiple reconstruction fraction, and the non-primary reconstruction fraction, respectively.

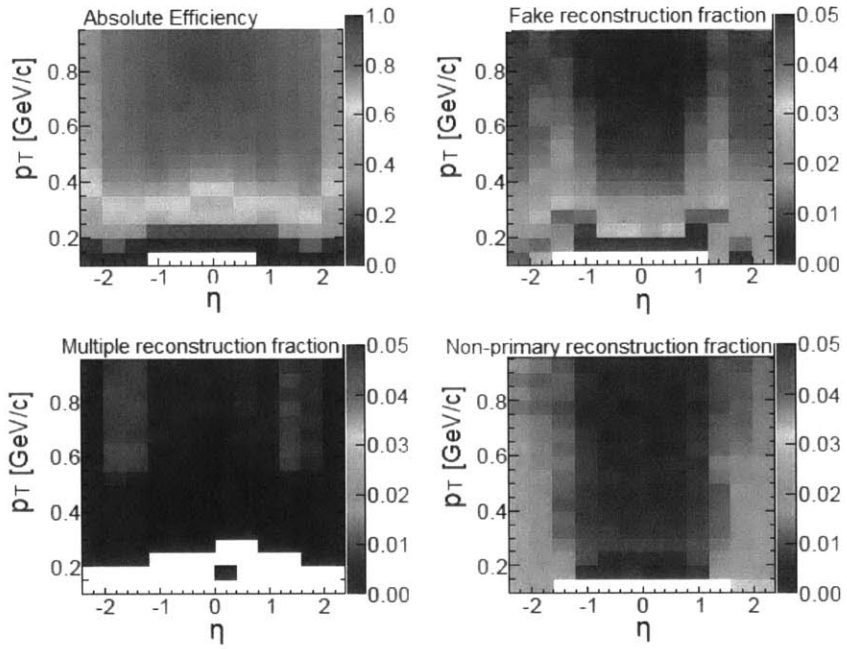

Figure 3-6: The same plots as in Figure 3-5 are shown, but zoomed in the p_T-axis.

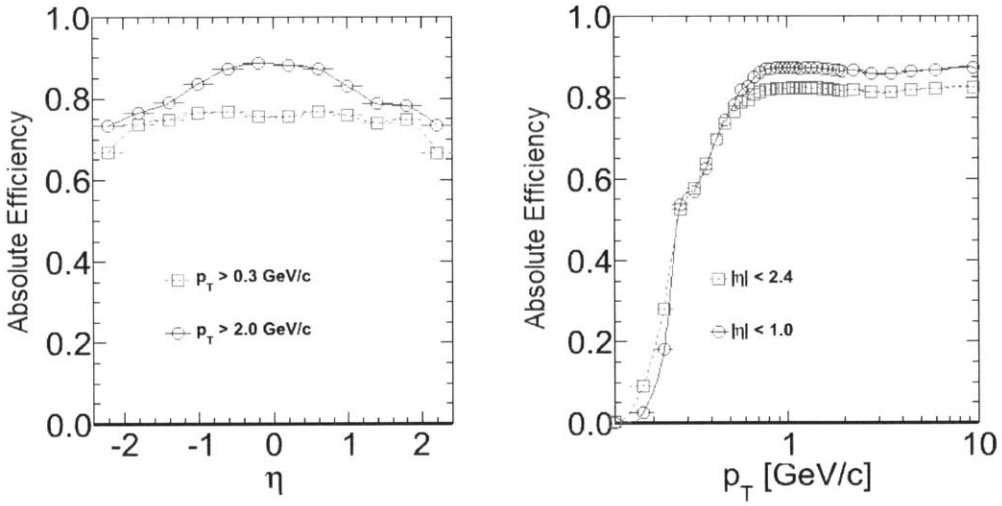

Figure 3-7: Projections of the tracking efficiency as a function of η (left) and p_T (right). The dashed line shows the lower p_T limit used in the analysis.

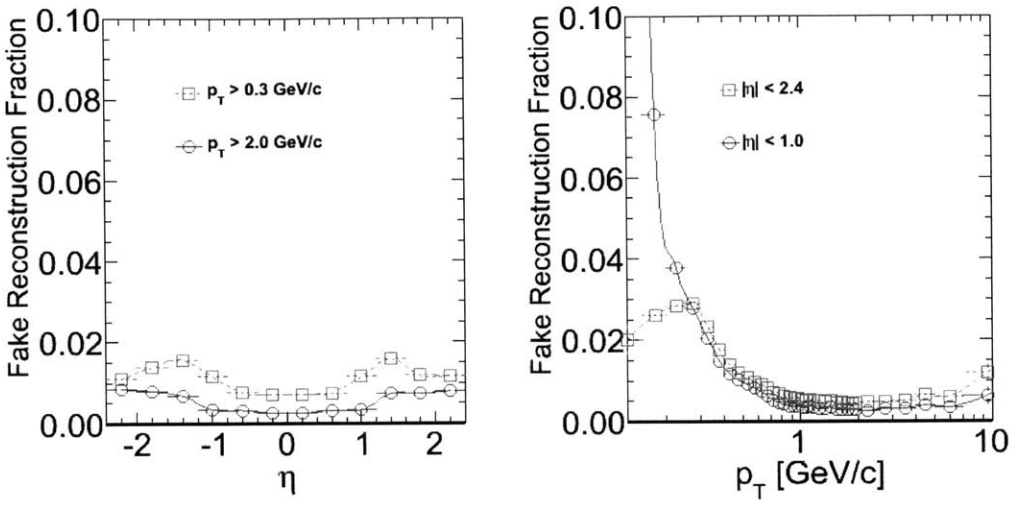

Figure 3-8: Projections of the fake track fraction as a function of η (left) and p_T (right). The dashed line shows the lower p_T limit used in the analysis.

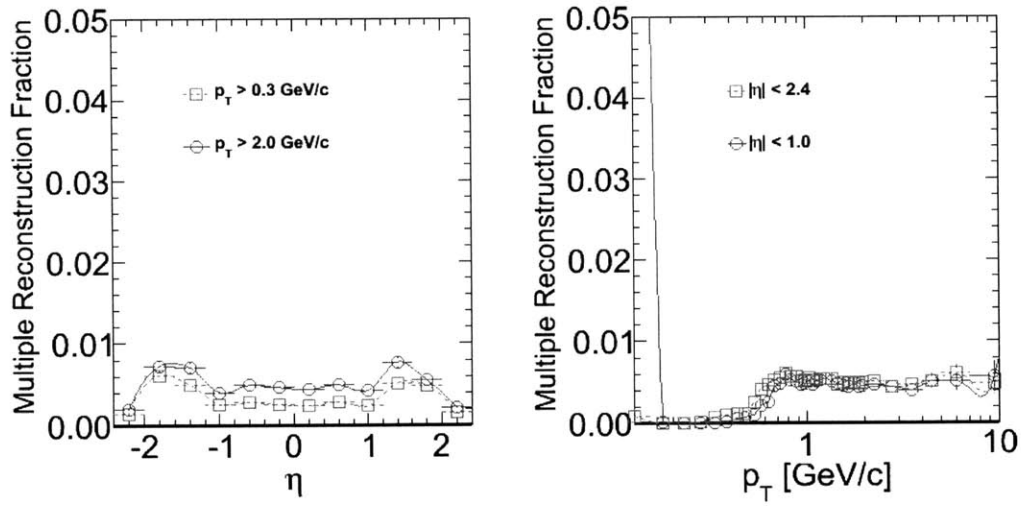

Figure 3-9: Projections of the multiple reconstruction fraction as a function of η (left) and p_T (right). The dashed line shows the lower p_T limit used in the analysis.

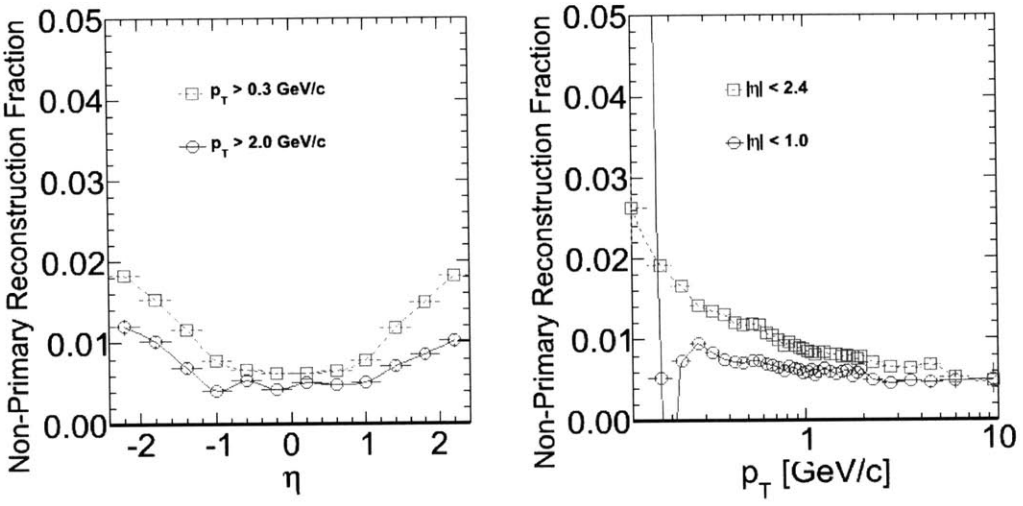

Figure 3-10: Projections of the non-primary reconstruction fraction as a function of η (left) and p_T (right). The dashed line shows the lower p_T limit used in the analysis.

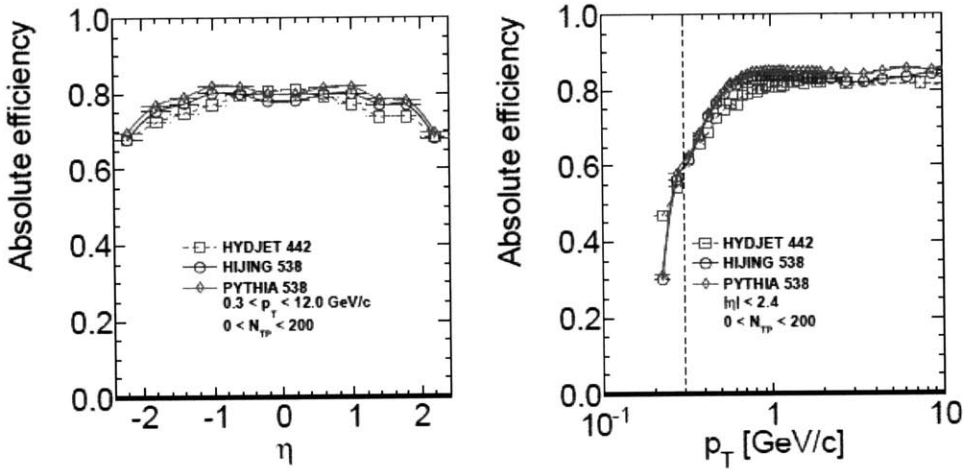

Figure 3-11: The absolute efficiencies calculated from HIJING (blue circles), PYTHIA (magenta diamonds), and HYDJET (red squares) are shown as a function of η for $0.3 < p_T < 12\ GeV/c$ (left) and p_T with $|\eta| < 2.4$ (right). The HYDJET calculation only includes events with $N_{TP} < 200$ (the number of simulated tracks in each event) for reasons discussed in the next section. Both HIJING and PYTHIA calculations were done in CMSSW 538patch3 and HYDJET was done in CMSSW 442patch5. The dashed line shows the lower p_T limit used in the analysis.

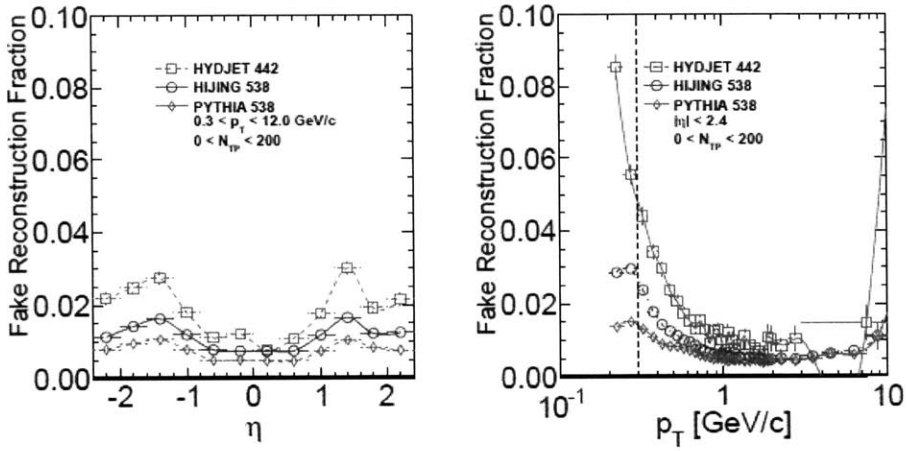

Figure 3-12: The fake rates calculated from HIJING (blue circles), PYTHIA (magenta diamonds), and HYDJET (red squares) are shown as a function of η for $0.3 < p_T < 12\ GeV/c$ (left) and p_T with $|\eta| < 2.4$ (right). The HYDJET calculation only includes events with $N_{TP} < 200$ (the number of simulated tracks in each event) for reasons discussed in the next section. Both HIJING and PYTHIA calculations were done in CMSSW 538patch3 and HYDJET was done in CMSSW 442patch5. The dashed line shows the lower p_T limit used in the analysis.

Chapter 4

Reconstruction of ϕ mass peak

4.1 Reconstruction of $\phi \rightarrow K^+K^-$ invariant mass peak

The ϕ-meson has a mean lifetime of $1.55 \pm 0.01 \times 10^{-22}s$. The implication of this is that by the time it has reached our detector, it has already decayed. So the only way of observing the signal of the ϕ-meson is to reconstruct its signal using its decay products or "daughter" particles. The most common decay mode of the ϕ-meson is its decay into pairs of oppositely charged Kaons, into which it decays almost 50% of the time. Since the mass of the ϕ is very close to the mass of two Kaons, this channel provides an extremely attractive way to obtain a mass peak distribution.

There are two challenges with using Kaons to reconstruct our ϕ-meson mass peaks. One is that we don't have perfect characterization of identified particles, so it is not always possible for us to say that a charged hadron (track) we observe in the detector is a Kaon. The other is that Kaons can be obtained from sources other than ϕ's. Our strategy, therefore is to consider all charged hadrons as possible "daughter particle" candidates from the ϕ when reconstructing its invariant mass peak.

The ϕ mass peak is reconstructed via the decay topology by combining pairs of oppositely charged tracks with an appropriate invariant mass. The two tracks are assigned Kaon mass, and their 4-vectors are combined to give the 4-vector of the ϕ candidate. This simple recipe gives us a distribution which looks like Figure 4-1. In the absence of background, we would expect our distribution to be centered roughly

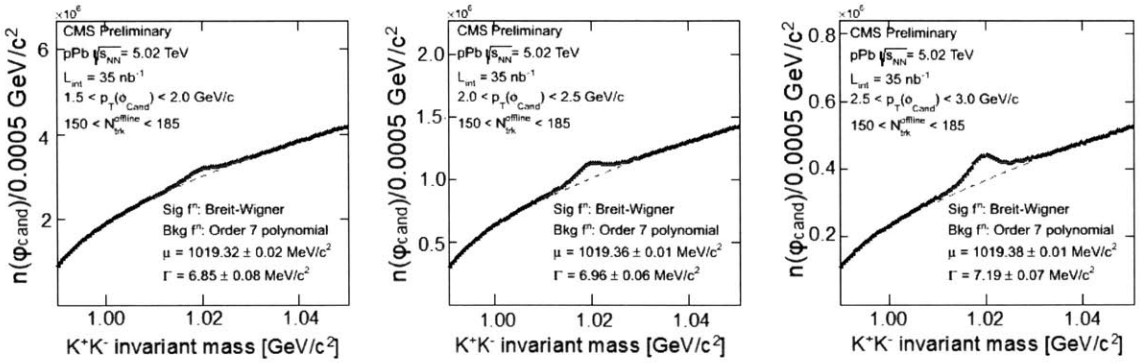

Figure 4-1: ϕ-meson invariant mass distributions in pPb collisions for the lower p_T bins used in this analysis

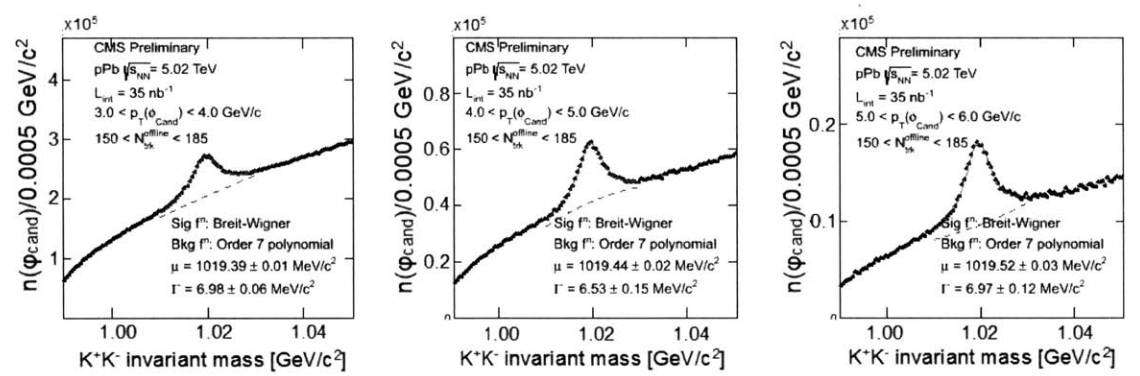

Figure 4-2: ϕ-meson invariant mass distributions for the higher p_T bins used in this analysis

at the PDG mass of the phi (1020 MeV/c^2), with flat tails on either side. However, as we mentioned earlier, the fact that we don't know which of our tracks are Kaons and whether or not they are daughters of a ϕ-meson results in us having a large combinatorial background on top of which this peak rests.

To model this distribution, we choose a relativistic Breit-Wigner distribution[42] on top of a 4th degree polynomial background. The choice of this function was dictated by a test of how well different functions performed when describing a Monte Carlo distribution for which we knew which Kaons were daughters of ϕ particles. The

Breit-Wigner distribution is a continuous probability distribution defined as

$$f(E) = \frac{k}{(E^2 - M^2)^2 + M^2\Gamma^2} \tag{4.1}$$

where k is a constant of proportionality equal to $k = \frac{2\sqrt{2}M\Gamma\gamma}{\pi\sqrt{M^2+\gamma}}$. The Breit-Wigner (BW) distribution is the function of choice to describe resonance of mesons, especially those in which broadening of the peak-width or a shift in the mass is expected to happen[43]. Another function we considered for this purpose was the Voigtian, which is the Breit-Wigner function convoluted with a Gaussian to model the broadening due to detector effects. However, it was found that the BW distribution performed better on Monte Carlo, and involved one less variable (the gaussian σ) which we had no control over, and hence was chosen.

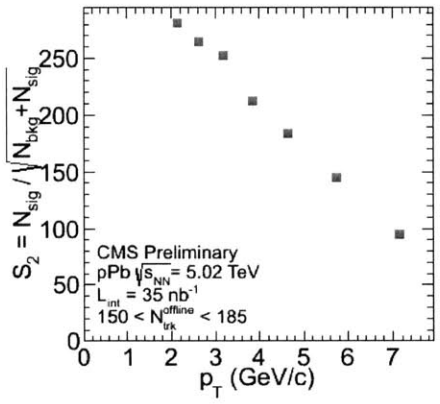

Figure 4-3: Signal significance of ϕ-mesons as a function of the transverse momentum p_T

The selection criteria outlined above are determined by optimizing the signal significance, $S/\sqrt{S+B}$, within $\pm 2\sigma$ mass window around the center of the mass peak. Here, S and B are numbers of signal and background candidates within selected mass windows, respectively. The signal significance, $S/\sqrt{S+B}$, and signal fraction, $S/S+B$, are shown in Figure 4-3 and Figure 4-4 respectively as a function of p_T, for pPb data at $\sqrt{s_{NN}} = 5.02TeV$ in multiplicity bin of $150 \leq N_{trk}^{off} < 185$.

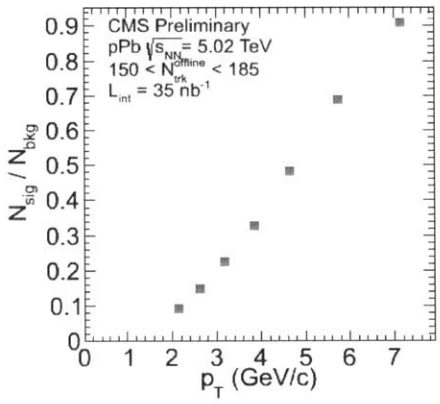

Figure 4-4: Signal/background ratio of ϕ-mesons as a function of the transverse momentum p_T

Chapter 5

Correlations and flow of ϕ mesons

The study of angular correlations of particles is a rich field which has provided a wealth of insight into the nature of the hot dense matter formed in heavy ion collisions as described in Section 1.3. To give a brief recap, when we talk of two-particle correlations, we usually mean angular correlations of pairs of particles in the $\Delta\eta - \Delta\varphi$ space. In the next few sections, we describe the technique of constructing and interpreting two-particle correlations, first in the general case, and then in the special case when our trigger particle is a resonance (like the ϕ meson) in our detector.

5.1 Two-Particle Angular Correlations

Two-particle correlation functions describe the likelihood of finding two particles at a given $\Delta\eta$ and $\Delta\varphi$ in our detector. Given the geometry of our detector, we are much more likely to find two particles close to each other in $\Delta\eta$ than very far apart. It is obvious that if we want to discover any novel phenomena, we will have to remove this bias. To this end, a technique called mixed event background subtraction is used. We construct a signal distribution, by correlating particles in a particular p_T range (which we tem as "trigger" particles) with all other particles in the same event (termed as "associated particles"). To model the background, we correlate trigger particles in one event, with associated particles in a different event, the idea being that particles in two different events cannot have any correlation with each other. The background

distribution we thus obtain represents effects we expect to see in the correlation function due to geometry alone (as described above). To obtain the final correlation function, we divide the signal distribution function by the background distribution function. To remove any biases that may occur in constructing our background function, we correlate events that occur at a very similar position (as measured with the z-coordinate of the collision vertex, v_z) in the detector and which produce a similar multiplicity of total particles. In addition, to construct the background function, each trigger particle is correlated with associate particles in ten other events.

For this particular analysis, the ϕ meson candidates are used as the trigger particles. The correlation function is constructed by counting the number of associated particles at a given $\Delta\eta$ and $\Delta\varphi$ from the trigger particle. Normalization of the correlation function is done in two steps. First, each entry in the histogram is weighted by the inverse of the number of trigger particles (N_{trig}) in the event. Then, the correlation function thus obtained after running over all the events is normalized by the total number of events to obtain the per-event per-trigger associated yield distribution, for trigger particles of the given p_T range. The per-trigger-particle associated yield distribution is thus defined by:

$$\frac{1}{N_{\text{trig}}}\frac{d^2N^{\text{pair}}}{d\Delta\eta d\Delta\varphi} = B(0,0) \times \frac{S(\Delta\eta,\Delta\varphi)}{B(\Delta\eta,\Delta\varphi)}, \tag{5.1}$$

where $\Delta\eta$ and $\Delta\varphi$ are the differences in η and ϕ of the pair, respectively. For the signal distribution, the trigger particle is correlated with all other charged hadrons in the p_T^{ass} range in the same event, except for the daughter tracks that went into its reconstruction. The signal distribution, $S(\Delta\eta,\Delta\varphi)$, is the measured per-trigger-particle distribution of same-event pairs, i.e.,

$$S(\Delta\eta,\Delta\varphi) = \frac{1}{N_{\text{trig}}}\frac{d^2N^{\text{same}}}{d\Delta\eta d\Delta\varphi}. \tag{5.2}$$

The mixed-event background distribution is calculated by correlating the trigger particle in an event with associated particles in 10 different events of similar z-vertex

and multiplicity. The mixed-event distribution is given by

$$B(\Delta\eta, \Delta\varphi) = \frac{1}{N_{\text{trig}}} \frac{d^2 N^{\text{mix}}}{d\Delta\eta d\Delta\varphi}, \tag{5.3}$$

The symbol N^{mix} denotes the number of pairs resulting from the event mixing. The normalization by N_{trig} of the background is performed for each event and then averaged over all the events, as in the case of the signal distribution.

The background distribution is used to account for random combinatorial background and pair-acceptance effects. The normalization factor $B(0,0)$ is the value of $B(\Delta\eta, \Delta\varphi)$ at $\Delta\eta = 0$ and $\Delta\varphi = 0$ (with a bin width of 0.3 in $\Delta\eta$ and $\pi/16$ in $\Delta\varphi$), representing the mixed-event associated yield for both particles of the pair going in approximately the same direction, thus having full pair acceptance. Therefore, the ratio $B(0,0)/B(\Delta\eta, \Delta\phi)$ is the pair-acceptance correction factor used to derive the corrected per-trigger-particle associated yield distribution. Equation (5.1) is calculated in 2 cm wide bins of the vertex position (z_{vtx}) along the beam direction and averaged over the range $|z_{\text{vtx}}| < 15$ cm.

An example of signal and background pair two-dimensional (2-D) distributions for ϕ-hadron correlations in $\Delta\eta$ and $\Delta\varphi$ is shown in Figure 5-1 for $4.2 < p_T < 5.1$GeV/c in $5.02TeV$ pPb data for $150 \leq N_{trk}^{off} < 185$. The triangular shape of the background distribution, shown in Figure 5-1(b) in $\Delta\eta$ is due to the limited acceptance in η such that the phase space for obtaining a pair at very large $\Delta\eta$ drops almost linearly toward the edge of the acceptance. Figure 5-1(c) shows the final correlation function that we obtain by conducting the mixed event background subtraction described above.

5.2 Azimuthal Anisotropy Harmonics from Two-Particle Correlations

To further quantify the correlation structure, the 2-D distributions are reduced to one-dimensional (1-D) distributions in $\Delta\varphi$ by averaging over the $\Delta\eta$ range [15, 14, 8, 9]. This is demonstrated in Figure 5-2.

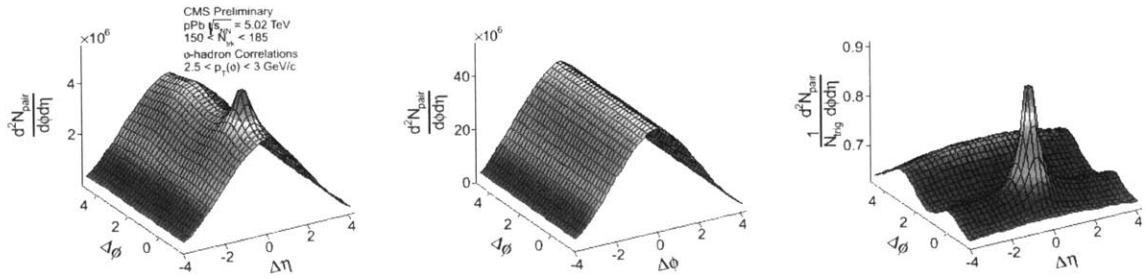

Figure 5-1: Signal, mixed-event background and correlation functions for ϕ-hadron correlations in the range 2.5 $GeV/c < p_T^{trg} < 3$ GeV/c, 0.4 $GeV/c < p_T^{ass} < 3$ GeV/c in 5.02 TeV pPb data with $150 \leq N_{trk}^{off} < 185$.

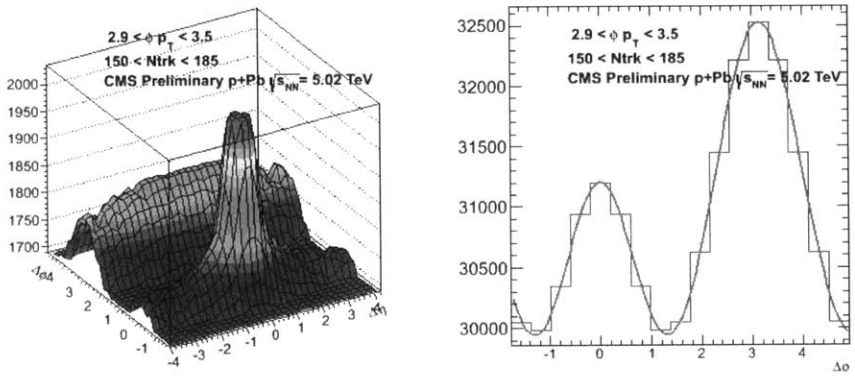

Figure 5-2: 2-D correlation functions are projected onto the $\Delta\varphi$ axis to extract the elliptic flow parameter v_2, which is simply the coefficient of the second Fourier component of the function

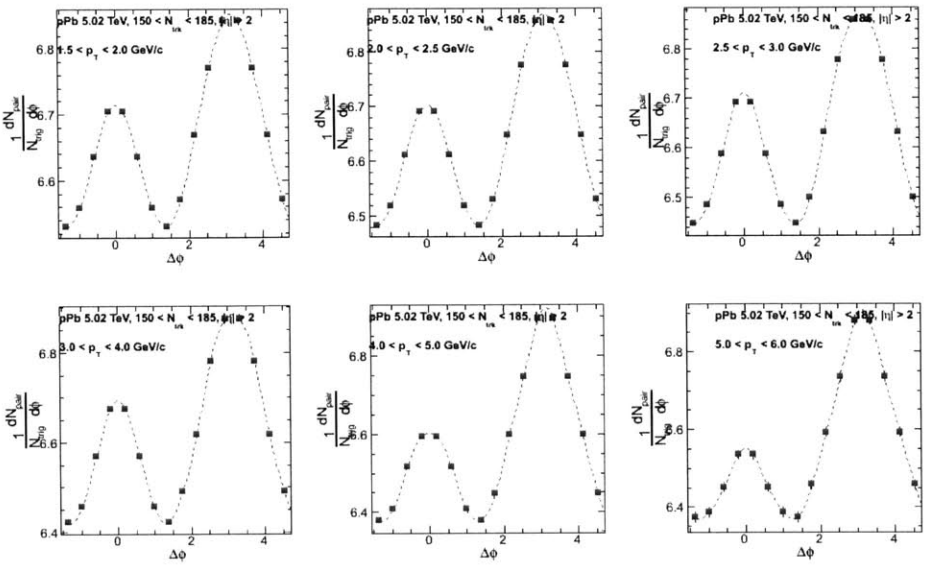

Figure 5-3: Projections to $\Delta\varphi$ of the correlation function in the range $|\Delta\eta| > 2$ for different p_T bins. The $cos(2\Delta\varphi)$ term gets more pronounced at higher p_T as can be seen by the growing asymmetricity of the two peaks.

The projections for different p_T bins for the multiplicity range [150,185) are shown in Figure 5-3.

The azimuthal anisotropy harmonics are determined from a Fourier decomposition of long-range (typically $|\Delta\eta| > 2$ to remove most of short-range correlations) two-particle $\Delta\phi$ correlation functions,

$$\frac{1}{N_{\rm trig}}\frac{\mathrm{N}^{\rm pair}}{d\Delta\phi} = \frac{N_{\rm assoc}}{2\pi}\left\{1 + \sum_n 2V_{n\Delta}\cos(n\Delta\phi)\right\}, \tag{5.4}$$

as described in Refs. [8, 9], where $V_{n\Delta}$ are the Fourier coefficients and $N_{\rm assoc}$ represents the total number of pairs per trigger particle for a given (p_T^{trg}, p_T^{ass}) bin. The first four Fourier terms are included in the fits. Including additional terms have negligible effects on the fit results. A minimum η gap of 2 units is applied to remove short-range correlations from jet fragmentation. The elliptic anisotropy harmonic, $v_2\{2, |\Delta\eta| > 2\}$ from two-particle correlation method can be extracted from the fitted Fourier coefficients as a function of p_T by assuming the factorization relation:

$$v_n\{2, |\Delta\eta| > 2\}(p_T) = \frac{V_{n\Delta}(p_T, p_T^{ref})}{\sqrt{V_{n\Delta}(p_T^{ref}, p_T^{ref})}}, \tag{5.5}$$

where n=2 for elliptic flow.

Here, a reference particle p_T^{ref} range is chosen to be $0.4 < p_T < 3.0$GeV/c. The $V_{n\Delta}(p_T^{ref}, p_T^{ref})$ is derived by correlating unidentified charged hadrons both from $0.4 < p_T < 3.0$GeV/c range (reference particles), while $V_{n\Delta}(p_T, p_T^{ref})$ represents Fourier coefficients by correlating a ϕ candidate with a reference particle.

5.3 Sideband subtraction method for eliminating background due to misreconstructed Kaon pairs

The v_2 calculated using the ϕ meson candidates requires a further step of background subtraction due to the contribution of the combinatorial background on top of which the ϕ meson mass peak rests. This contribution is described by the simple relation

$$v_n^{true} = \frac{N_{\text{signal}} v_n^{massband} - N_{\text{background}} v_n^{sideband}}{N_{\text{signal}} N_{\text{background}}} \tag{5.6}$$

N_{signal} and $N_{\text{background}}$ are estimated by integrating under the peak region for the peak and background distributions respectively. The contribution to v_2 of the ϕ meson background is estimated from the sidebands. The assumption is that the particles under the background distribution can be estimated by looking at the background distribution far away from the peak region. For the purpose of this analysis, the mass band is taken as the region $\mu \pm 0.5\Gamma$. For the sideband region, we construct a distribution of v_2 vs. the invariant mass of the ϕ-candidate, and fit it with a straight line far away from the mass region. The statistical uncertainty on the fit gives us the statistical uncertainty on our sideband region.

An illustration of the sidebands and mass band is given in Figure 5-4. An example plot of v_2 vs. mass used to calculate the sideband v_2 is shown in Figure 5-5, while a plot demonstrating the typical values of v_2 before and after subtraction is shown in

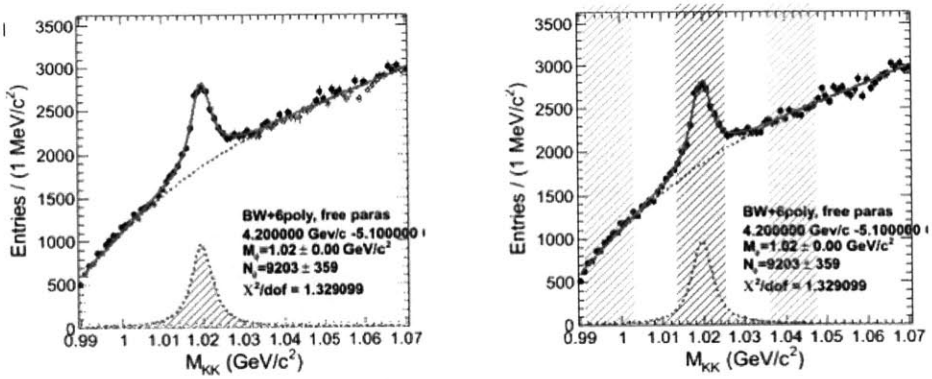

Figure 5-4: Sideband subtraction method: The central (darker) blue shaded region is the mass band while the two (lighter) green shaded regions are the two sidebands.

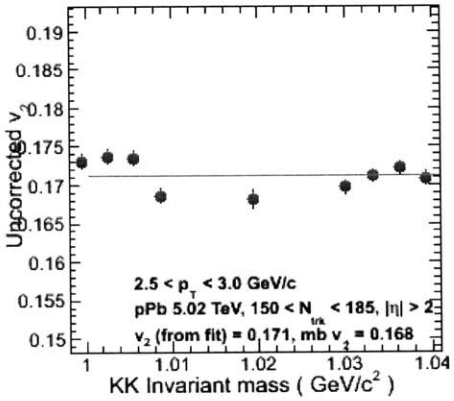

Figure 5-5: v_2 vs. invariant mass plot used to calculate sideband v_2. Since the value of the sideband v_2 varies with mass, we fit it with a straight line in regions far away from the mass peak to obtain the value used for calculating the final v_2 value of ϕ-mesons

Figure 5-6.

Propagation of uncertainties of v_n^{sig}

The Fourier coefficients $V_{n\Delta}$ and their uncertainties $\Delta V_{n\Delta}$ are extracted from the Fourier decomposition fits of two-particle $\Delta\varphi$ correlation functions. Some notations are defined as follow:

- V_n^{ref}, ΔV_n^{ref}: V_n coefficients and uncertainties of hadron-hadron correlations.
- V_n^{obs}, ΔV_n^{obs}: V_n coefficients and uncertainties of V^0-hadron correlations from peak region.

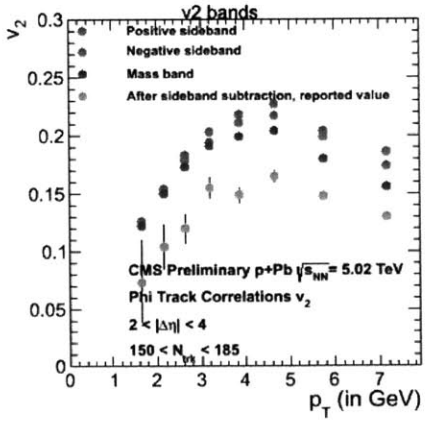

Figure 5-6: This figure displays the intermediate values used in calculating the ϕ-meson v_2. The two sidebands have a higher v_2 at all values of p_T than the mass band. It follows logically that the final background subtracted value of the ϕ-meson v_2 is thus lower than all the other three.

- V_n^{bkg}, $\Delta V_n^{\mathrm{bkg}}$: V_n coefficients and uncertainties of V^0-hadron correlations from background region.

The v_n^{ref} for reference particles as well as it uncertainty is derived as

$$v_n^{\mathrm{ref}} = \sqrt{V_n^{\mathrm{ref}}}, \tag{5.7}$$

and

$$\Delta v_n^{\mathrm{ref}} = \frac{1}{2}\sqrt{V_n^{\mathrm{ref}}}\frac{\Delta V_n^{\mathrm{ref}}}{V_n^{\mathrm{ref}}}. \tag{5.8}$$

The v_n^{obs} and v_n^{bkg} and their uncertainties are calculated as

$$v_n^{\mathrm{obs,bkg}} = \frac{V_n^{\mathrm{obs,bkg}}}{v_n^{\mathrm{ref}}}, \tag{5.9}$$

and

$$\Delta v_n^{\mathrm{obs,bkg}} = v_n^{\mathrm{obs,bkg}}\sqrt{\left(\frac{\Delta V_n^{\mathrm{obs,bkg}}}{V_n^{\mathrm{obs,bkg}}}\right)^2 + \left(\frac{\Delta v_n^{\mathrm{ref}}}{v_n^{\mathrm{ref}}}\right)^2}, \tag{5.10}$$

Chapter 6

Systematic uncertainties and cross checks

In any experimental measurement, uncertainties appear due to an inherent inaccuracy of the experimental apparatus. In our measurement, the apparatus in question is the CMS detector and most of our systematic uncertainties arise because of inherent inaccuracies in the measurement of the position and momentum of particles in the detector subsystems. In particular, for this analysis, this manifests itself in our ability to know which of the ϕ-meson candidates we reconstruct are the real ϕs and which are a result of the combinatorial background. We account for the error introduced due to this by considering various sources of systematic uncertainty, and quoting the final result with this error, in addition to the statistical uncertainty.

6.1 Systematic uncertainty due to choice of fit range

As mentioned in the previous sections, we obtain a distribution of ϕ-candidates by constructing an invariant mass distribution from the sum of 4-momenta of oppositely charged hadrons. For the calculation of v_2, we need to estimate the number of ϕ-mesons in the "peak region". To this end, we must fit the distribution obtained with a function, and integrate under the peak to count the number of ϕs. As explained in the previous section, our distribution of choice to model the signal is a relativistic

Breit-Wigner distribution, while we model the combinatorial background on which this peak sits, by a 4th order polynomial. Systematic error is introduced when we choose what mass range we choose as the range of our fit function. The trade-off here is between choosing a very small region around the peak to accurately model the peak, but then we run the risk of not taking into account the shape of the background correctly. Conversely, if we choose too wide a range, we risk including the low-mass region which is not as well-defined by virtue of being too close in value to the sum of mass of two Kaons. The results of this systematic study are presented in Figure 6-1.

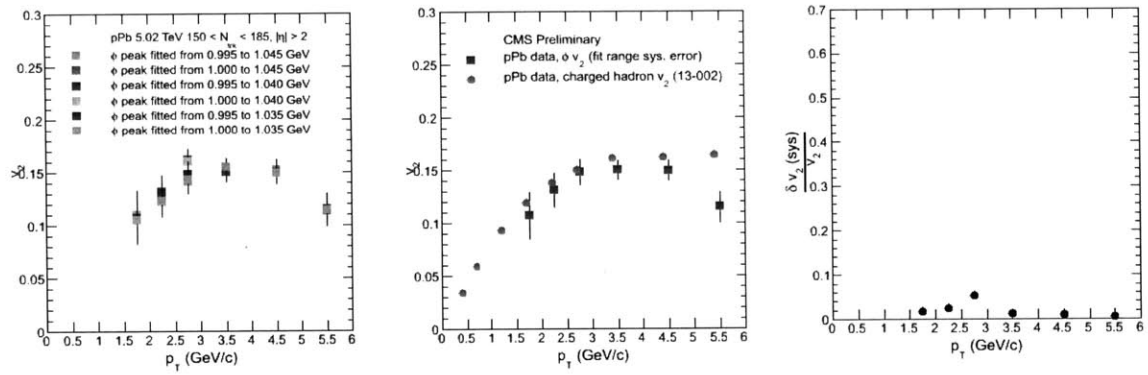

Figure 6-1: Plots demonstrating the systematic uncertainty due to choice of ϕ peak fit range are shown here. The leftmost plot shows the values of the ϕ-meson v_2 plotted for 6 cases where the invariant mass peak was fitted over different ranges. The middle plot compares the value of the ϕ v_2 to that of all hadrons. The rightmost plot shows the relative systematic uncertainty introduced by varying our choice of fit range.

6.2 Systematic uncertainty due to choice of sideband region

In the previous chapter, we described the side-band subtraction technique to obtain the v_2 of identified particles. Another source of systematic uncertainty is the choice of the region we consider as the "sideband". Put differently, there is expected to be some variation in the v_2 of the sidebands, depending on how far away from the ϕ peak you choose your sideband to be. To quantify this uncertainty, a systematic study was conducted, and the final v_2 values were calculated using the v_2 vs Mass fit

in different sideband regions. The standard deviation of these values contributes to the systematic uncertainty. The results are presented in Figure 6-2.

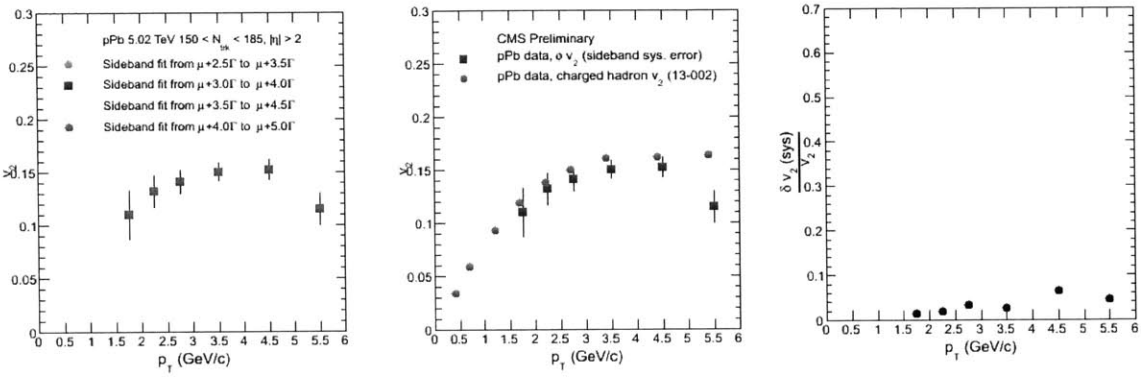

Figure 6-2: Plots demonstrating the systematic uncertainty due to choice of sideband region are shown here. The leftmost plot shows the values of the ϕ-meson v_2 plotted for 4 cases, where different regions in the invariant mass distributions were used to calculate the sideband v_2 using the method described in Chapter 5. The middle plot compares the value of the ϕ v_2 to that of all hadrons. The rightmost plot shows the relative systematic uncertainty introduced by varying our choice of sideband region.

6.3 Systematic uncertainty due to choice of peak region width

This source of systematic uncertainty is related to the one presented in the previous section. It is not possible to make a definitive statement about where the peak region ends, and the sideband region begins. Depending on how many decay widths we go away from the peak, we include more and more of the background in what we would consider to be our signal region. We have flexibility in choosing how wide we want to make our "peak region" and "sideband region", but this too contributes to the overall systematic uncertainty. For this study, we varied our choice of the peak region width from $\mu \pm 0.25\Gamma$ to $\mu \pm Gamma$ and collated the results as the final number that we put on the systematic uncertainty. A summary of this study is shown in Figure 6-3.

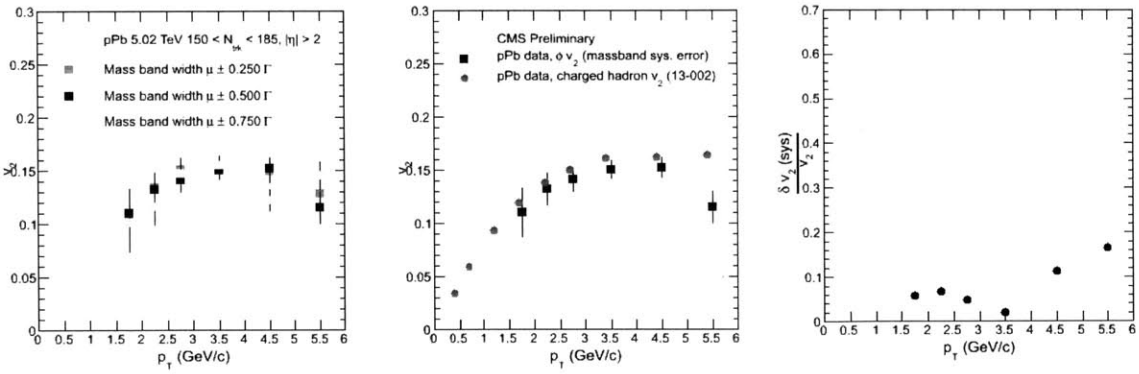

Figure 6-3: Plots demonstrating the systematic uncertainty due to choice of the width of the mass band region are shown here. The leftmost plot shows the values of the ϕ-meson v_2 plotted for 3 cases, where we choose to include different sizes of areas around the peak into our definition of the mass band region. The middle plot compares the value of the ϕ v_2 to that of all hadrons. The rightmost plot shows the relative systematic uncertainty introduced by varying our choice of the width of the peak or the mass band region.

6.4 Monte Carlo closure study

One of the most important cross-checks when conducting an experimental high energy physics measurement, is to compare the generator level truth of Monte Carlo simulations to the values obtained by running the simulation through the detector and measuring the observed values, as one would for real data. We call this the Monte Carlo closure study. Since our systematic uncertainties are being introduced due to imperfect reconstruction of the ϕ-meson distribution, we calculate the values of systematic error due to imperfect Monte Carlo closure by comparing the yields of the generator level ϕ-meson distribution to the reconstructed ϕ distribution. The results of this study are presented in Figure 6-4.

6.5 Summary of sources of systematic uncertainties

All the sources of systematic uncertainty are summarized in Table 6.1 and displayed in Fig 6-5. The overall systematic uncertainty was found to be of the same order as that of the statistical uncertainty for the range of multiplicity and transverse momenta presented here. This suggests that our results in this reason are well constrained.

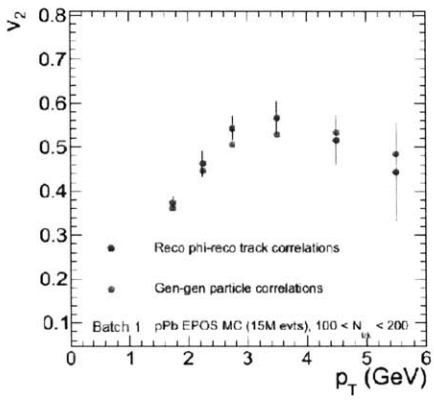

Figure 6-4: Monte-Carlo closure study using EPOS-LHC Monte Carlo to compare v_2 of ϕ's known from the generator-level truth to v_2 calculated using $\phi \to K^+K^-$ peak reconstruction, following the method used for experimental data.

Table 6.1: Summary of systematic uncertainties on v_2 in pPb collisions.

Source	
mass band region range	6.0%
Sideband region range	3.0%
Mass distribution fit range	3.0%
MC closure	5.0%
Total	8.9%

Chapter 7 deals with a more elaborate description of these results and their implications.

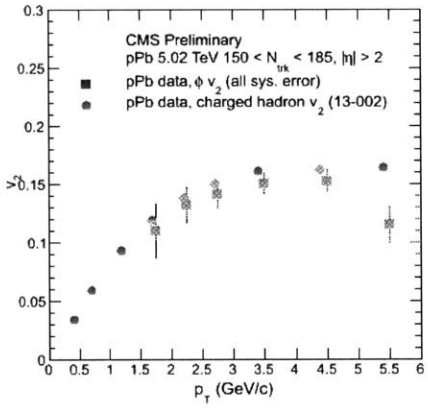

Figure 6-5: ϕ-meson v_2 results shown with systematics errors (yellow boxes) and statistical error bars.

Chapter 7

Results

7.1 Results and Discussion

Correlation functions of ϕ-mesons with charged hadrons in pPb collisions with the CMS detector show the same long-range near-side ridge observed for correlations of pairs of charged hadrons in high multiplicity pp, pPb and PbPb collisions.

As described in chapter 5, the strength of these correlations can be quantified in terms of the elliptic flow coefficients v_2. By comparing the values of v_2 as a function of the transverse momentum, of ϕ-mesons to other identified particles, we can test the predictions of quark number scaling and mass ordering which were described in Chapter 1.

Figure 7-1 shows the values of ϕ-meson v_2 compared to a previous measurement of the v_2 of all charged hadrons by the CMS experiment[20] and the v_2 of K_s and $\Lambda/\bar{\Lambda}$ particles. As stated in Chapter 1, the measurement of azimuthal anisotropy of identified particles can shed light upon the mechanism driving the "flow" of these particles in the QGP[44]. As can be seen, the v_2 of the ϕ is consistently smaller than that of all charged hadrons. If we believe in the mass ordering effect of the flow coefficients, this should not be surprising, since most charged hadrons produced in particle collisions are light pions and Kaons.

The comparison the ϕ v_2 to the v_2 of K_s and $\Lambda/\bar{\Lambda}$ particle species can help us further explore the mass ordering effect and also the hypothesis of quark number

scaling. If we see the v_2 values for all three identified particle species, it is clear that at low p_T values, the K_s which has the lowest mass of about half a GeV has the highest v_2, while the Λ and the ϕ, which have masses slightly in excess of 1 GeV are very close together in value. Further, we can see that at p_T's higher than GeV, the v_2 of the Λ, which is a baryon rockets far above the v_2 of the ϕ and K_s mesons. The implication being that at higher p_T's, the quark number scaling effect dominates over mass ordering. This mass ordering effect suggests that the elliptic flow is built up in the early partonic stage of the evolution of the fireball, while the quark number scaling effect implies that the scattering that takes place post-hadronization. Figure 7-2 compares the values of v_2 when scaled by the number

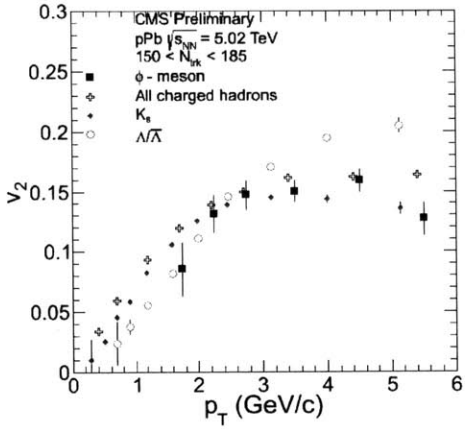

Figure 7-1: The elliptic flow coefficient (v_2) as a function of the transverse momentum of ϕ mesons is compared to that of K_s, $\Lambda/\bar{\Lambda}$, and all charged hadrons for $150 < N_{trk}^{off} < 185$ for proton-Lead collisions at a center-of-mass energy of 5.02 TeV as measured by the CMS experiment at the Large Hadron Collider.

of constituent quarks versus the transverse kinetic energy scaled by the number of constituent quarks $(m_T - m)/n_q$ of ϕ, K_s, and $\Lambda/\bar{\Lambda}$ particles. It is found that above 1 GeV, the v_2 of the ϕ-meson is consistent with the quark number scaling hypothesis as predicted by quark-coalescence models. One implication of this might be that the hadronic interaction cross-section of the ϕ has been underestimated by theoretical calculations. As stated earlier, the quark number scaling effect is thought to arise from quark coalescence and rescattering post-hadronization. If the ϕ did in fact have a very low cross-section of interaction, then we would expect it to have a very low v_2

at higher p_T's too, as a result. But as can be seen from the quark number scaling v_2 plots, this is clearly not the case.

Certain hybrid models predict that mass ordering will be violated for ϕ-mesons due to the high strangeness content and low hadronic cross-section of interaction of the ϕ [45]. However, within the limits of our uncertainties, ϕ.-mesons seem to follow the mass ordering behavior.

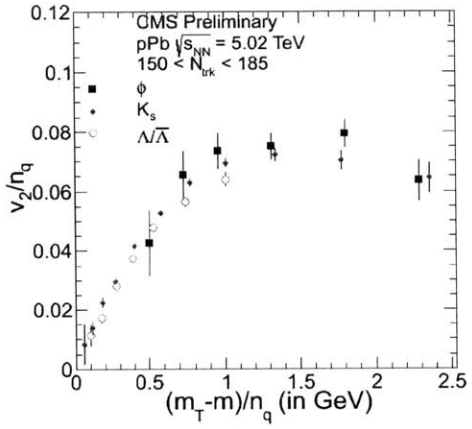

Figure 7-2: To test the quark number scaling hypothesis of the elliptic flow (v_2) of ϕ, K_s and $\Lambda/\bar{\Lambda}$ particles, both the p_T and v_2 of identified particle species are scaled by the number of their constituent quarks. The values for mesons - ϕ and K_s line up, while the $\Lambda/\bar{\Lambda}$ seem to follow a different curve. Results are presented for a multiplicity range $150 < N_{trk}^{off} < 185$ for pPb collisions at a center-of-mass energy of 5.02 TeV measured by the CMS experiment at CERN.

Similar studies on the flow of identified particles, and the ϕ in particular, have been conducted with Au-Au collisions at RHIC by the STAR and PHENIX experiments, and more recently with the ALICE experiment at the LHC[46]. Figure 7-3 details the v_2 of various identified particles. It can be seen that these results too follow the mass ordering effect at low p_T and quark number scaling at higher p_T, thus affirming that the mechanism that gives rise to these effects in pPb and PbPb collisions is very similar, if not the same.

7.2 Outlook

The ϕ-meson as a probe of heavy ion physics has a vast potential for differentiating models of evolution and development of the post-collision system. In this thesis, we hae demonstrated the validity of the quark number scaling property of the elliptic flow of hadrons. However, the precision of the measurement is limited by the large background of the ϕ meson. Higher statistics from future runs will definitely play a factor in reducing the statistical error bars. Using identified Kaons at low p_T, it should be possible to reduce the background of the ϕ peak and gain further accuracy on our measurements. The interplay of the dual effects of mass ordering and quark number scaling observed in pA and AA collisions is never clearer than in measurements of the ϕ's properties, and further studies would greatly increase out understanding of the evolution and formation of the QGP in heavy ion collisions.

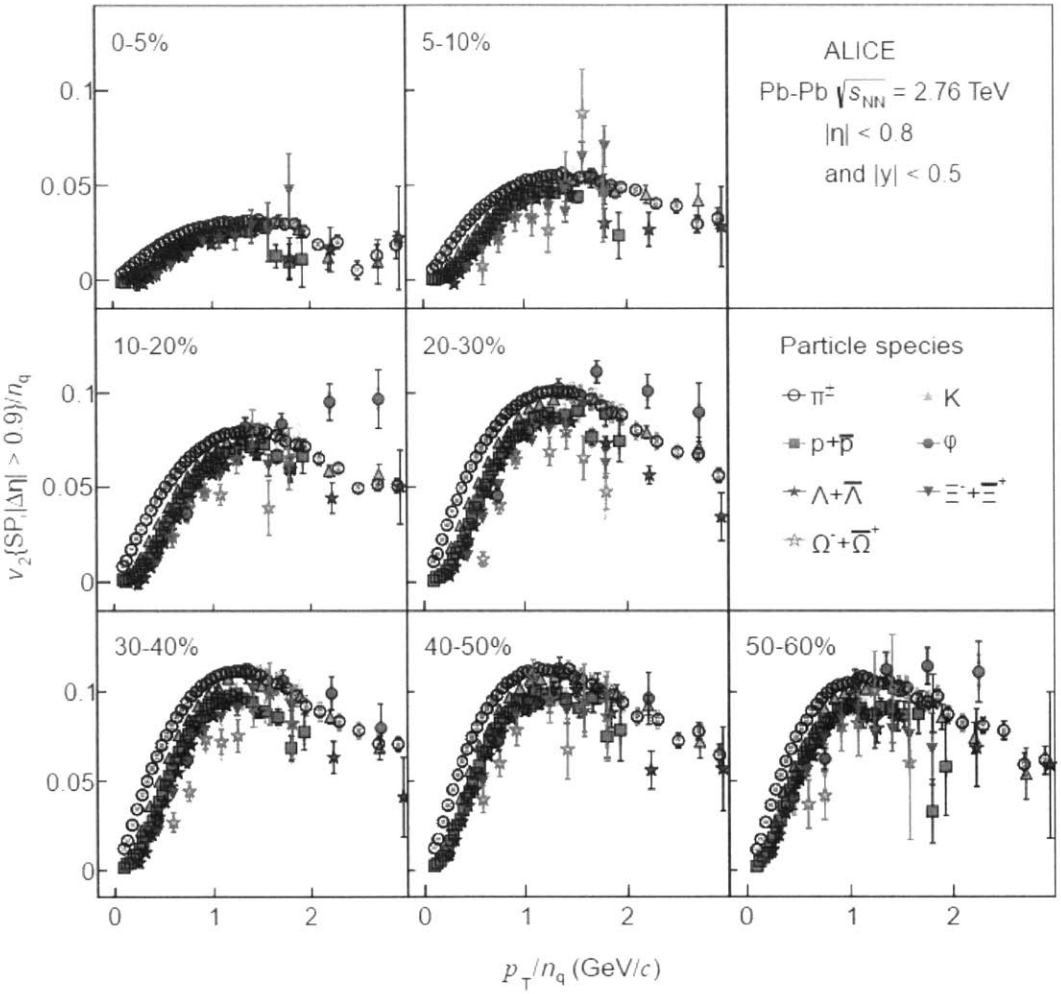

Figure 7-3: v_2/n_q of different identified particle species as a function of p_T/n_q for different centralities in Pb-Pb collisions as measured by the ALICE collaboration. It is clear that there is a quark number scaling effect at play here, as well as mass ordering, as evidenced by the higher values of the v_2 of π^0

Bibliography

[1] K.A. Olive et al. Review of particle physics. *Chin.Phys.*, C38:090001, 2014.

[2] Siegfried Bethke. The 2009 world average of α_s. *Eur. Phys. J. C*, 64:689–703, 2009.

[3] J. Adams et al. Distributions of charged hadrons associated with high transverse momentum particles in pp and Au + Au collisions at $\sqrt{S_{NN}}$ = 200GeV. *Phys. Rev. Lett.*, 95:152301, 2005.

[4] B.I. Abelev et al. Long range rapidity correlations and jet production in high energy nuclear collisions. *Phys. Rev. C*, 80:064912, 2009.

[5] B. Alver et al. System size dependence of cluster properties from two- particle angular correlations in Cu+Cu and Au+Au collisions at $\sqrt{S_{NN}}$ = 200GeV. *Phys. Rev. C*, 81:024904, 2010.

[6] B. Alver et al. High transverse momentum triggered correlations over a large pseudorapidity acceptance in Au+Au collisions at $\sqrt{S_{NN}}$ = 200GeV. *Phys. Rev. Lett.*, 104:062301, 2010.

[7] B. I. Abelev et al. Three-particle coincidence of the long range pseudorapidity correlation in high energy nucleus-nucleus collisions. *Phys. Rev. Lett.*, 105:022301, 2010.

[8] Serguei Chatrchyan et al. Long-range and short-range dihadron angular correlations in central PbPb collisions at a nucleon-nucleon center of mass energy of 2.76 TeV. *JHEP*, 07:076, 2011.

[9] Serguei Chatrchyan et al. Centrality dependence of dihadron correlations and azimuthal anisotropy harmonics in PbPb collisions at $\sqrt{S_{NN}}$ = 2.76 TeV. *Eur. Phys. J. C*, 72:2012, 2012.

[10] K. Aamodt et al. Harmonic decomposition of two-particle angular correlations in Pb-Pb collisions at $\sqrt{S_{NN}}$ = 2.76TeV. *Phys. Lett. B*, 708:249, 2012.

[11] Georges Aad et al. Measurement of the azimuthal anisotropy for charged particle production in $\sqrt{S_{NN}}$ = 2.76TeV lead-lead collisions with the ATLAS detector. *Phys. Rev. C*, 86:014907, 2012.

[12] Serguei Chatrchyan et al. Studies of azimuthal dihadron correlations in ultra-central PbPb collisions at $\sqrt{S_{NN}}$ = 2.76TeV. *JHEP*, 02:088, 2014.

[13] Jean-Yves Ollitrault. Anisotropy as a signature of transverse collective flow. *Phys. Rev. D*, 46:229, 1992.

[14] Vardan Khachatryan et al. Observation of Long-Range Near-Side Angular Correlations in Proton-Proton Collisions at the LHC. *JHEP*, 09:091, 2010.

[15] Serguei Chatrchyan et al. Observation of long-range near-side angular correlations in proton-lead collisions at the LHC. *Phys. Lett. B*, 718:795, 2013.

[16] Betty Abelev et al. Long-range angular correlations on the near and away side in pPb collisions at $\sqrt{S_{NN}}$ = 5.02TeV . *Phys. Lett. B*, 719:29, 2013.

[17] Georges Aad et al. Observation of Associated Near-side and Away-side Long-range Correlations in $\sqrt{S_{NN}}$ = 5.02TeV Proton-lead Collisions with the ATLAS Detector. *Phys. Rev. Lett.*, 110:182302, 2013.

[18] S. Voloshin and Y. Zhang. Flow study in relativistic nuclear collisions by Fourier expansion of azimuthal particle distributions. *Z. Phys. C*, 70:665, 1996.

[19] Wei Li. Observation of a 'Ridge' correlation structure in high multiplicity proton-proton collisions: A brief review. *Mod. Phys. Lett. A*, 27:1230018, 2012.

[20] CMS Collaboration. Long-range two-particle correlations of strange hadrons with charged particles in ppb and pbpb collisions at LHC energies. *Phys. Lett. B*, 742(200), 2015.

[21] Betty Bezverkhny Abelev et al. Long-range angular correlations of pi, K and p in p–Pb collisions at $\sqrt{S_{NN}}$ = 5.02TeV. *Phys. Lett. B*, 726:164, 2013.

[22] John Adams et al. Experimental and theoretical challenges in the search for the quark gluon plasma: The STAR Collaboration's critical assessment of the evidence from RHIC collisions. *Nucl. Phys. A*, 757:102, 2005.

[23] K. Adcox et al. Formation of dense partonic matter in relativistic nucleus-nucleus collisions at RHIC: Experimental evaluation by the PHENIX collaboration. *Nucl. Phys. A*, 757:184, 2005.

[24] S.S. Adler et al. Elliptic flow of identified hadrons in Au+Au collisions at $\sqrt{S_{NN}}$ = 200-GeV. *Phys. Rev. Lett.*, 91:182301, 2003.

[25] J. Adams et al. Azimuthal anisotropy in Au+Au collisions at $\sqrt{S_{NN}}$ = 200-GeV. *Phys. Rev. C*, 72:014904, 2005.

[26] P. Huovinen, P.F. Kolb, Ulrich W. Heinz, P.V. Ruuskanen, and S.A. Voloshin. Radial and elliptic flow at RHIC: Further predictions. *Phys. Lett. B*, 503:58, 2001.

[27] Peter F. Kolb and Ulrich W. Heinz. Hydrodynamic description of ultrarelativistic heavy ion collisions. 2003.

[28] Chun Shen, Ulrich Heinz, Pasi Huovinen, and Huichao Song. Radial and elliptic flow in Pb+Pb collisions at the Large Hadron Collider from viscous hydrodynamic. *Phys. Rev. C*, 84:044903, 2011.

[29] K. Werner, M. Bleicher, B. Guiot, Iu. Karpenko, and T. Pierog. Evidence for flow in pPb collisions at 5 TeV from v_2 mass splitting. 2013.

[30] Piotr Bozek, Wojciech Broniowski, and Giorgio Torrieri. Mass hierarchy in identified particle distributions in proton-lead collisions. *Phys. Rev. Lett.*, 111:172303, 2013.

[31] B.I. Abelev et al. Mass, quark-number, and $\sqrt{s_{NN}}$ dependence of the second and fourth flow harmonics in ultra-relativistic nucleus-nucleus collisions. *Phys. Rev. C*, 75:054906, 2007.

[32] A. Adare et al. Deviation from quark-number scaling of the anisotropy parameter v_2 of pions, kaons, and protons in Au+Au collisions at $\sqrt{S_{NN}} = 200$ GeV. *Phys. Rev. C*, 85:064914, 2012.

[33] Denes Molnar and Sergei A. Voloshin. Elliptic flow at large transverse momenta from quark coalescence. *Phys. Rev. Lett.*, 91:092301, 2003.

[34] V. Greco, C.M. Ko, and P. Levai. Parton coalescence and anti-proton / pion anomaly at RHIC. *Phys. Rev. Lett.*, 90:202302, 2003.

[35] R.J. Fries, Berndt Muller, C. Nonaka, and S.A. Bass. Hadronization in heavy ion collisions: Recombination and fragmentation of partons. *Phys. Rev. Lett.*, 90:202303, 2003.

[36] Vardan Khachatryan et al. Transverse momentum and pseudorapidity distributions of charged hadrons in pp collisions at sqrt(s) = 0.9 and 2.36 TeV. *JHEP*, 02:041, 2010.

[37] CMS Collaboration. Multiplicity and transverse momentum dependence of two and four-particle correlations in ppb and pbpb collisions. *Phys. Lett. B*, 724(213), 2013.

[38] D. Giordano and G. Squazzoni. CMS reconstruction improvements for the tracking in large pile-up events. *Journal of Physics: Conference Series*, 396(022044), 2012.

[39] CMS Collaboration. Measurement of the inelastic ppb cross section at 5.02 tev. CMS Physics Analysis Summary CMS-PAS-FSQ-13-006, 2013.

[40] Studies of two-particle correlations in ppb collisions at 5tev. Technical report, 2012.

[41] CMS Collaboration. Tracking and vertexing results from first collisions. CMS Physics Analysis Summary CMS-PAS-TRK-10-001, 2010.

[42] F. James. *Statistical Methods in Experimental Physics*. World Scientific.

[43] Torbjorn Sjöstrand, Stephen Mrenna, and Peter Skands. PYTHIA 6.4 Physics and Manual; v6.420, tune D6T. *JHEP*, 05:026, 2006.

[44] P. F. Kolb, P. Huovinen, Ulrich W. Heinz, and H. Heiselberg. Elliptic flow at SPS and RHIC: From kinetic transport to hydrodynamics. *Phys. Lett.*, B500:232–240, 2001.

[45] D. Kharzeev R. Lacey T. Hirano, U. Heinz and Y. Nara. Mass ordering of differential elliptic flow and its violation for phi mesons. *Phys. Rev. C*, 77:044909, 2008.

[46] ALICE Collaboration. Elliptic flow of identified hadrons in pb-pb collisions at $\sqrt{s_{NN}} = 2.76$ tev. 2014.